

“© 2020 IEEE. Personal use of this material is permitted. Permission from IEEE must be obtained for all other uses, in any current or future media, including reprinting/republishing this material for advertising or promotional purposes, creating new collective works, for resale or redistribution to servers or lists, or reuse of any copyrighted component of this work in other works.”

UDR: An Approximate Unbiased Difference-Ratio Edge Detector for SAR Images

Qian-Ru Wei, Da-Zheng Feng, *Member, IEEE*, and Wen-Jing Jia

Abstract—Edge detection is a critical component of synthetic aperture radar (SAR) image interpretation. Due to serious speckle noise, the core problems for SAR edge detection are how to keep a constant false alarm rate and how to achieve unbiased localization of the edges. Aiming at these problems, this paper proposes a novel edge detector with a unique structure for noise-contaminated SAR images, which creatively integrates the difference operation with ratio operation (hence named as “UDR : Unbiased Difference-Ratio” edge detector). Theoretical analysis proves that the difference operation effectively affords the UDR unbiased localization ability for both ideal and non-ideal edges, and the ratio operation provides the UDR the property of constant false alarm rate under the influence of speckle noise. Experimental results on both simulated and real-world SAR images demonstrate the unbiased localization ability of the proposed UDR edge detection, insensitive to the changes of edge contrast, the width of the transition zone and the noise level. Benefited from the superior localization precision and insensitivity to noise, the average true positive detection rate of the proposed detector is improved to 95%, outperforming the compared state-of-the-art methods.

Index Terms—Edge Detector, Non-ideal Step Edge, Unbiased Localization, Constant False Alarm Rate, Synthetic Aperture Radar (SAR), Difference Operation, Ratio Operation.

I. INTRODUCTION

WITH the rapid development of synthetic aperture radar (SAR) technology, an enormous amount of methods [1], [2], [3], [4] have been proposed for detecting edges from SAR images. As a critical step of SAR image processing and interpretation, the performance of SAR image edge detection, including computational complexity, accuracy, robustness etc., directly affects or even determines the performance of many applications. For example, Tu and Su [5] suggested a fast and accurate target detection method which utilized the outcome of an SAR edge detector to modify the total variation energy in order to obtain a robust result. Liu et al. [2] proposed an automatic method to detect the border of ice, which took edge-based region generation as its initial step. To predict the movement of oil spills, Li et al. [6] adopted images’ edge maps to assimilate the geometric information of the observed images. Xu et al. [7] used edge as a penalty to increase the classification accuracy of remote sensed images. Besides aforementioned examples, there are

dozens more similar examples reported in literatures [8], [9]. All these examples show that accurate edge detection has always been and will continue to be a critical step for SAR image processing and interpretation.

For many image processing or analysis applications, edge detection is a valuable and fundamental step. Due to the complexity of various surfaces in the scene, an image usually contains multiple types of edges, including ridge edge, step edge, ramp edge [11], roof edge [10], etc. In this paper, we focus on the problem of detecting step edge from SAR images because the step edges are the predominant ones in SAR images. The profile of an ideal step edge looks like a stair step. In 2D space the step edge can be defined as the local maximum of gradient magnitude in the normal direction [12].

Optical images usually contain unignorable additive white Gaussian noise [13]. Hence, the difference operation is naturally adopted to calculate the gradient magnitude for efficiently extracting edges in images. SAR images are obtained from the coherent imaging system and hence contain serious speckle noise. Speckle noise is generally modeled as multiplicative noise, which is signal-dependent and cannot be neglected [14]. Multiplicative noise is the main reason that makes edge detectors based on difference operation lose their constant false alarm rate (CFAR) property [14]. To address the problem caused by speckle noise, pre-filtering is the most widely used approach. By estimating or transforming, pre-filtering approaches obtain a denoise SAR image [42]. This kind of approaches more or less cause the loss of some of the information of the original SAR image, resulting in the distortion and loss of edge features. Unfortunately, such distortion and loss of edge features may not be easily rectified or recovered. In this paper, we focus our work on how to directly extract edge features from SAR images so as to avoid the drawbacks of pre-filtering.

A. Related Works

During the last twenty years, many specialized SAR edge detection methods have been proposed [14], [15], [16], [17]. Since speckle noise visually degrades the quality of SAR images and largely increases the difficulty of edge detection, most methods are mainly concerned with how to effectively detect edges with improved detection rate [17].

Improving the detection rate includes both decreasing the false-positive (FP) rate and increasing the true-positive (TP) rate. The improvement in detection rate will largely help to improve the performances of corresponding methods. Taking the application of image registration [18], [19] as an example,

Qian-Ru Wei was with the School of Software and Microelectronics, Northwestern Polytechnical University, Xi’an, 710072, China; e-mail: (weiqianru_123@163.com).

Da-Zheng Feng is National Laboratory of Radar Signal Processing, Xidian University, Xi’an, China.

Wen-Jing Jia, corresponding author, is Global Big Data Technologies Centre, University Technology Sydney, Sydney, Australia.

Manuscript received 2018; revised August 26, 2018.

higher FP rates tend to lead to a large number of outliers, whereas low TPs result in reduced number of usable points for registration. Popular approaches used to decrease the FP rate includes enhancing the anti-noise ability of detectors and reducing the width of the resultant edge [25]. As for increasing the TP rate, commonly used methods include changing the shape and size of the filter, adding post-processing operations and enhancing edge continuity [24]. Furthermore, a new research indicates that the localization accuracy of a detector has a significant impact on the detection rate. Improving the localization accuracy can reduce edge distortion, thus helping detector to achieve high detection rate. Due to relatively complex implementation, such a method is rare in SAR edge detection.

Commonly used SAR edge detection methods can be roughly categorized as *heuristic methods* and *filtering methods*.

The *heuristic methods* are mainly based on the global statistical features of SAR images. In this group of methods, one of the best known and widely used edge detection algorithms is the active contour method [23]. The active contour method determines edges by performing one (or more) cost function optimization on the seed points. This method iteratively minimizes the cost function until a satisfactory detection result is achieved. The heuristic methods can obtain good detection accuracy, which is one of the main advantages of this type of method. However, as pointed out in [20][21], a set of seed points with ‘good’ initialization position must be provided for fast convergence and good detection results. Additionally, the optimization needs a number of iterations. This results in that the heuristic methods are usually computationally expensive [13], which can affect the real-time performance of the relevant applications. Due to these drawbacks, the heuristic methods are not discussed in this paper. Readers interested in this type of detectors may refer to the classical references by Oliver [22], Vincent and Soille [23], and Germain and Rfrgier [24].

The *filtering methods* are based on the local spatial characteristics of SAR images. The advantages of such methods are easy implementation, reliable detection, simple structure and low computational complexity. Furthermore, under the multiplicative noise model [28], [29], such methods can maintain a constant false alarm rate. The filtering approach proposed by Touzi in [14] is a milestone in the study of SAR edge detection. The approach is named as the Ratio of Averages (ROA) which consists of two stages. First, an edge strength map is computed by a bi-window rectangle filter. Then, a post-processing using the Non-maximum Suppression and Hysteretic Threshold (NSHT) [12][16] algorithm is performed to suppress and extract false and true edge pixels from the edge strength map. Actually, most of the filtering methods use a unified framework which is congruent with the ROA. That is to say, filtering methods usually include a detection filter and a post-processing method. As a common and famous post-processing extraction method, the NSHT has been adopted by many filtering methods. Besides the NSHT, several commonly used edge-pixel extraction methods, such as watershed algorithm in combination with thresholding of the basin dynamics or region merging and so on [26][27], can be used to replace the NSHT. For a more detailed discussion

on post-processing methods, we refer readers to [16][17] and the references therein.

For the *filtering methods*, their filters have direct impacts on their detection results. The bi-window rectangle filter of the ROA approach applies to detect edges complying with ideal monoedge model [15][17]. For detecting edges that obey the multiedge model, exponential (1D infinite symmetric exponential filter)-Gaussian-shaped filter [22] introduced by Fjrtoft should be used to compute the ratio of exponentially weighted averages (ROEWA). To further improve the detection performance of ROA with low FP rates, Shui et al. introduced a detector with Gaussian-Gamma-Shaped (GGG) filter for achieving edges with only one-pixel width [16]. Due to speckle noise and other factors, in practice, edges are usually non-ideal rather than ideal. In consideration of this, Wei et al. [17] proposed an efficient Ratio-Based Edge Detector (RBED). The detection filter adopted by the RBED is the product of a 1D power modulated Gaussian vertical filter and a 1D flat bell-shaped parallel filter. The RBED applies to edges that obey non-ideal step edge model and has a low false positive rate. The filtering methods generally adopt same detection structures for performing ratio operation to achieve a constant false alarm rate. Hence, a more common name for the filtering methods is ratio-based edge detectors.

B. Motivation

The filtering methods have several desirable advantages. However, one of the drawbacks of such methods is that ratio operation results in the localization bias for non-ideal edges. When a ratio-based edge detector detects an ideal edge, if the filter orientation does not coincide with the edge direction, the edge position estimated by this detector becomes slightly biased [27][30]. In this case, if we perform the detection with filters of several different directions, the bias can usually be limited within an acceptable level [17][27][30]. When a ratio-based edge detector detects a non-ideal edge, typical for SAR images contaminated by speckle noise, even if the filtering orientation coincides with the edge direction, the edge position estimated by the detector is biased [17]. Even worse, the intensity of the bias increases with the increase of edge contrast and transition size. For ratio-based edge detectors, the bias caused by non-ideal edges cannot be easily controlled or eliminated. Localization bias is the major reason why image segmentation algorithms usually choose heuristic methods, instead of filtering methods, to refine their segmentation results [31], [32]. Therefore, how to design an edge detector with good localization ability for non-ideal edges becomes an urgent problem in theoretical research for SAR image edge detection.

The challenges encountered to solve this problem are unprecedented. As aforementioned, for non-ideal step edges in SAR images, the ratio-based edge detectors can preserve constant false alarm rate but tend to have biased localization. Interestingly, through our repeated experiments and strict theoretical proof, we found that difference-based edge detectors can provide unbiased edge location for non-ideal edges. However, the difference-based edge detectors cannot maintain

constant false alarm rate [14] under the multiplicative noise model and therefore they cannot be directly used for SAR images.

In this paper, aiming to improve the detection rate from the aspect of localization accuracy, we propose an optimal, unbiased edge detector to address the edge detection problem of non-ideal edges in SAR images. Different from the traditional filtering methods, our proposed detector adopts a unique structure which creatively integrates the difference operation with ratio operation. To the best of our knowledge, such a special structure has never been reported anywhere in related literatures. We named the proposed detector as Unbiased Difference-Ratio edge detector, abbreviated as ‘‘UDR’’ edge detector hereafter for simplicity. Our UDR edge detector provides optimal localization precision for non-ideal step edges and maintains constant false alarm rate under the multiplicative noise model. Theoretic analytical calculation and subjective and objective experimental results demonstrate that the proposed UDR edge detection algorithm possesses the characteristic of precise localization, robust to noise and can achieve smooth and closed skeleton edges. Furthermore, our UDR can achieve high true positive rates with low false positives. To further simplify the proposed detector, a simplified version of UDR is also proposed. Theoretical analysis shows that the simplified version of UDR can significantly save the complex computation while achieving the same performance as the full version UDR.

The contributions of this paper include:

- 1) In order to address the edge detection problem of non-ideal edges in SAR images, a novel, unbiased edge detector ‘‘UDR’’ is proposed which creatively integrates the difference operation with ratio operation in a unique structure.
- 2) Theoretical analytical calculations show that the special structure makes the UDR detector possess the desired properties of unbiased localization and constant false alarm rate in the context of speckle noise.
- 3) Additional structure simplification is achieved through theoretical analysis. The simplification largely reduces the computational complexity of the methods.
- 4) Qualitative and quantitative experiments demonstrate that the optimal unbiased edge localization ability of the proposed method, which is insensitive to the changes of edge contrast, transition zone width and noise intensity.

This rest of the paper is organized as follows. In Section II, we introduce the multiplicative noise model and illustrate how to estimate the parameter related to the scattering coefficient from the multiplicative noise model. The estimated parameter is required by the UDR edge detector. Section III shows the formulation of the UDR algorithm and theoretically analyzes the characteristics of the proposed UDR edge detector. Furthermore, in Section III, a simplified version of UDR is proposed and its computational complexity is also analyzed. Comparative experimental results are presented in Sections IV. Finally, the paper concludes in Section V.

II. THE MULTIPLICATIVE NOISE MODEL

For the cases of fully developed speckle noise, a SAR image I can be modeled by the multiplicative noise model as [14], [33], [34]:

$$I = R \cdot \zeta, \quad (1)$$

where R is the cross-section (backscatter) of the illuminated target and ζ is the speckle noise. Note that R and ζ are mutually independent. For clear distinction, we use the subscripts ‘ A ’ and ‘ B ’ to denote the amplitude and intensity respectively.

The probability density function (PDF) of I_A is written as:

$$f_{I_A}(I) = \frac{2(L/\lambda)^L}{\Gamma(L)} I^{2L-1} \exp(-\frac{L}{\lambda} I^2), \quad I > 0. \quad (2)$$

Here, $\Gamma(\bullet)$ is the gamma function, $L > 0$ is the number of look, λ is proportional to scattering coefficient. Equation (2) is the distribution of homogeneous region. Its derivation is given in references [28], [29], [33]. For simplicity, Equation(2) is denoted by the notation $I_A \sim \Gamma^{1/2}(L, L\lambda)$. This notation is first used in reference [28].

According to Equation (2), the k -order moment of I_A is given by:

$$\begin{aligned} m_k &= \int_0^{+\infty} I^k \frac{2(L/\lambda)^L}{\Gamma(L)} I^{2L-1} \exp(-LI^2/\lambda) dI \\ &= \frac{2}{\Gamma(L)} \int_0^{+\infty} (L/\lambda)^L I^{2L+k-1} \exp(-LI^2/\lambda) dI \\ &= \frac{2}{\Gamma(L)} \int_0^{+\infty} U^{2L+k-1} \exp(-U^2) (L/\lambda)^{-k/2} dU \\ &= (L/\lambda)^{-k/2} \frac{\Gamma(L+k/2)}{\Gamma(L)}. \end{aligned} \quad (3)$$

where $U = (L/\lambda)^{1/2} I$.

Let $I_i, i = 1, 2, \dots, N$ be a random variable in a homogeneous region. All variables I_i coming from the same homogeneous area can be assumed to be independent and identically distributed [14]. If the variables have a distribution of $I_i \sim \Gamma^{1/2}(L, L\lambda)$, its k -order sample moment is defined as [39]:

$$\widehat{m}_k = N^{-1} \sum_{i=1}^N I_i^k. \quad (4)$$

Combining Equations (3) and (4), the parameter λ in Equation (2) can be estimated. For example, if the one-order moment m_1 and the one-order sample moment \widehat{m}_1 are used, the parameter λ is given by:

$$\widehat{\lambda} = L \left[\frac{\widehat{m}_1 \cdot \Gamma(L)}{\Gamma(L+1/2)} \right]^2, \quad (5)$$

where $\widehat{\lambda}$ is the estimated λ . Here, the number of look L is generally known. If we do not know the value of L , it can be easily estimated beforehand by several methods [35][36]. The estimated L is valid for the whole image. Actually, through the analysis shown in the following section, we know that our method is unrelated to L . Therefore, L does not need to be specially estimated.

As for the intensity format of the SAR image, I_B , we have $I_B = R_B \cdot \zeta_B = R_A^2 \cdot \zeta_B$ [28]. Hence, the distribution of the intensity homogeneous region and its related parameters can be easily estimated by the method similar to $I_A \sim \Gamma^{1/2}(L, L\lambda)$. Applying analogous analysis to the intensity image, one can easily obtain the parameter estimation method (detector) for the intensity images. If the one-order moment m_1 and the one-order sample moment \widehat{m}_1 are used, the parameter λ in the distribution of I_B is $\widehat{\lambda} = \widehat{m}_1 L \Gamma(L) / \Gamma(L + 1)$. Different parameter estimation methods mean detection method for amplitude and intensity images should be different. Due to limited space, the detector proposed in this paper only applies for amplitude images. Readers interested to intensity images processing can adopt the same unique structure to design an unbiased edge detector for intensity SAR images.

III. THE UNBIASED DIFFERENCE-RADIO (UDR) EDGE DETECTOR

A. The Formulation of UDR

The proposed UDR includes a 2D separable edge detection filter, which consists of two orthogonal 1D filters, one vertical filter $h_{UDR}^\perp(x)$ and one parallel filter $h_{UDR}^\parallel(y)$. The biggest advantage of using two 1D filter to combine a 2D filter is convenient to design the 2D filter [43]. For the sake of a clear distinction, we use $h_{name}(x, y)$ to denote a filter, where the subscript denotes the name of the filter. The direction of the filter is displayed in superscript. The superscripts ' \parallel ' and ' \perp ' denote the parallel and vertical respectively. The 1D vertical filter $h_{UDR}^\perp(x)$ is written as:

$$\begin{aligned} h_{UDR}^\perp(|x|) &= |x|^{\alpha-1} \exp\left(-\frac{|x|}{\beta}\right) \\ &= h_{UDR}^\perp(x) + h_{UDR}^\perp(-x) \end{aligned} \quad (6)$$

where $h_{UDR}^\perp(x) = |x|^{\alpha-1} \exp\left(-\frac{|x|}{\beta}\right) \varepsilon(x)$ and $h_{UDR}^\perp(-x) = |x|^{\alpha-1} \exp\left(-\frac{|x|}{\beta}\right) \varepsilon(-x)$. Parameters $\alpha > 1$ and $\beta > 0$ in Equation (6) controls the peak values and attenuation speed of the vertical filter. The $\varepsilon(\bullet)$ represents Heaviside function. The 1D parallel filter $h_{UDR}^\parallel(y)$ is written as:

$$h_{UDR}^\parallel(y) = \begin{cases} 1 & |y| \leq l_\parallel \\ \exp\left(-\frac{(|y|-l_\parallel)^2}{2\sigma_\parallel^2}\right) & |y| > l_\parallel \end{cases}. \quad (7)$$

Equation (7) shows that the $h_{UDR}^\parallel(y)$ is a flat bell shaped function. Its performance has been analyzed in [17] in detail. Parameters l_\parallel and σ_\parallel represent flat and attenuation parameters, respectively. The 2D edge detection filter of UDR is written as:

$$\begin{aligned} h_{UDR}(x, y) &= h_{UDR}^\perp(|x|) h_{UDR}^\parallel(y) \\ &= \bar{h}_{UDR}(x, y) + \underline{h}_{UDR}(x, y) \end{aligned} \quad (8)$$

where $\underline{h}_{UDR}(x, y) = h_{UDR}^\perp(-x) h_{UDR}^\parallel(y)$ and $\bar{h}_{UDR}(x, y) = h_{UDR}^\perp(x) h_{UDR}^\parallel(y)$ are the left and right parts of the filter $h_{UDR}(x, y)$, respectively. It is worth to note that usually The

effective support area of a nonnegative 2D filter is defined as the ratio of its 2D integration to its maximum value [17]. The $h_{UDR}(x, y)$ with a large effective support area can efficiently increase the ability for resisting noise and smoothing edges. Considering the characteristics of step-edges, the effective support area of $h_{UDR}(x, y)$ should be restricted to a moderate size.

In digital SAR images, $h_{UDR}(x, y)$ generates a sliding window with two sub-regions, in which the $\underline{h}_{UDR}(x, y)$ and $\bar{h}_{UDR}(x, y)$ separately confirm the left and right sub-regions. Clearly, the sliding window width and the spacing of two sub-regions are controlled by the two adjustable parameters α and β in Equation (6), while the sliding window length of the UDR is jointly controlled by the two adjustable parameters l_\parallel and σ_\parallel in Equation (7). The weight of sliding window is proportional to the filter coefficient. Furthermore, by considering the characteristics of digital images, the sliding window needs to be truncated and sampled at the grids of the image. Figure 1 shows the profile of a sliding window generated by $h_{UDR}(x, y)$.

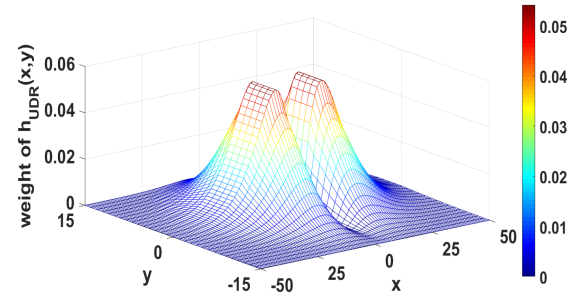


Fig. 1. Profile of the weight map of $h_{UDR}(x, y)$.

Using the generated sliding window, the strength $S_{UDR}(x, y)$ of pixel (x, y) is computed by:

$$\begin{aligned} S_{UDR}(x, y) &= \frac{|I(x, y) \otimes \bar{h}_{UDR}(x, y) - I(x, y) \otimes \underline{h}_{UDR}(x, y)|}{\sqrt{\bar{\lambda}(x, y) + \underline{\lambda}(x, y)}} \\ &= \frac{|\bar{Z}_{UDR}(x, y) - \underline{Z}_{UDR}(x, y)|}{\sqrt{\bar{\lambda}(x, y) + \underline{\lambda}(x, y)}} \end{aligned} \quad (9)$$

where \otimes denotes the convolution operation. The local weighted averages $\underline{Z}_{UDR}(x, y) = I(x, y) \otimes \underline{h}_{UDR}(x, y)$ and $\bar{Z}_{UDR}(x, y) = I(x, y) \otimes \bar{h}_{UDR}(x, y)$ correspond to the left and right sub-windows, respectively. In digital images, the convolution operation can be realized by the Hadamard product or the Fourier transform [44]. Of course, it is only the different ways to implement the convolution operation rather than different methods to compute the local weighted averages. The estimated scattering parameters $\underline{\lambda}(x, y)$ and $\bar{\lambda}(x, y)$ are estimated by the samples coming from the left sub-region of the sliding window and the right sub-region of the sliding window, respectively. The estimated method is described in Equation (5) in detail (see Section 2).

In order to match edges with an orientation of θ , $h_{UDR}(x, y)$ is rotated to the direction θ . The rotated filter is denoted as $h_{UDR}^\theta(x, y)$, calculated as:

$$h_{UDR}^\theta(x, y) = \underline{h}_{UDR}^\theta(x, y) + \bar{h}_{UDR}^\theta(x, y) \quad (10)$$

where $\bar{h}_{UDR}^\theta(x, y) = \bar{h}_{UDR}(x \cos \theta - y \sin \theta, x \sin \theta + y \cos \theta)$ and $\underline{h}_{UDR}^\theta(x, y) = \underline{h}_{UDR}(x \cos \theta - y \sin \theta, x \sin \theta + y \cos \theta)$. At θ direction, the strength $S_{UDR}^\theta(x, y)$ of the pixel (x, y) can be computed by:

$$S_{UDR}^\theta(x, y) = \frac{|\bar{Z}_{UDR}^\theta(x, y) - \underline{Z}_{UDR}^\theta(x, y)|}{\sqrt{\bar{\lambda}^\theta(x, y) + \underline{\lambda}^\theta(x, y)}} \quad (11)$$

where $\bar{Z}_{UDR}^\theta(x, y) = I(x, y) \otimes \bar{h}_{UDR}^\theta(x, y)$ and $\underline{Z}_{UDR}^\theta(x, y) = I(x, y) \otimes \underline{h}_{UDR}^\theta(x, y)$; $\bar{\lambda}^\theta(x, y)$ and $\underline{\lambda}^\theta(x, y)$ are estimated by using the rotated sliding window.

If θ in Equation (10) continuously changes, the UDR edge detector will have the capability of detecting edges along arbitrary directions. Considering the tradeoff between computational complexity and detection accuracy, θ is taken as several discrete directions only [12]. That means the angle precision of the UDR edge detector is dependent on the number of discrete directions [17].

The edge strength of one pixel is obtained by applying the detection filter of several different orientations and fusing their strength statistically. According to Equation (11), the edge strength map (ESM) of the image $I(x, y)$, denoted as $ESM_{UDR}(x, y)$, is obtained by:

$$ESM_{UDR}(x, y) = \max_{k=0,1,\dots,M-1} S_{UDR}^{\theta_k}(x, y) \quad (12)$$

where $\theta_k = k\pi/M$ and M is the number of orientations. The variable $k = 0, 1, \dots, M-1$ is the index of orientations. And, the edge direction map (EDM) of the image, denoted as $EDM_{UDR}(x, y)$, is:

$$EDM_{UDR}(x, y) = \arg \max_{\theta_k} S_{UDR}^{\theta_k}(x, y) + \pi/2. \quad (13)$$

The proposed UDR can effectively detect edges by performing a 2D edge detection filtering, a scattering parameter estimation, and a post-processing edge extraction operations in turn. That means, following the operations defined in Equations (12) and (13), the NSHT operation is performed on the resultant $ESM_{UDR}(x, y)$ and $EDM_{UDR}(x, y)$ to generate a binary edge map for the image $I(x, y)$. NSHT includes two parts non-maximum suppression and hysteretic thresholding. The non-maximum suppression is operated on each $ESM_{UDR}(x, y)$ along the direction $EDM_{UDR}(x, y)$ to judge if $ESM_{UDR}(x, y)$ is a maximum. All maxima in the ESM form the candidate set of edge pixels. Then, hysteretic thresholding is used to extract true edge pixels from the candidate set. Let us perdefine two thresholds T_{low} and T_{high} ($T_{low} < T_{high}$). A pixel in the candidate set with edge strength no less than T_{high} is marked as a strong pixel. A pixel in the candidate set with edge strength between T_{low} and T_{high} is marked as a weak pixel. All strong pixel are declared as edge

pixels. A weak pixel is declared as an edge pixel only when there is an edge pixel in its four- or eight-neighborhood.

B. Constant False Alarm Rate

The PDF of a homogeneous pixel X has distribution of $x \sim \Gamma^{1/2}(L, L\sigma_0)$, where x is a random pixel value, L denotes the number of looks, and σ_0 is the scattering coefficient. Let $Y = X/Q$, where Q is a positive constant, and we can deduce the PDF of Y as:

$$f_Y(y) = \frac{2}{\Gamma(L)} \left(Q^2 \frac{L}{\sigma_0}\right)^L y^{2L-1} \exp(-Q^2 \frac{L}{\sigma_0} y^2) \quad (14)$$

where y is a random variable.

Let Z be the local weighted average of N homogenous pixels, i.e., $Z = \sum_{i=1}^N X_i/Q_i = \sum_{i=1}^N Y_i$, where all X_i are independently and identically distributed and all Q_i are positive constants. The PDF of variable Z recorded as $f_Z(z)$ is computed by:

$$G_Z(\omega) = \prod_{i=1}^N \int_{-\infty}^{+\infty} e^{i\omega y} f_Y(y) dy \quad (15)$$

$$= \prod_{i=1}^N \int_{-\infty}^{+\infty} \frac{2e^{i\omega y}}{\Gamma(L)} \left(\frac{Q_i^2 L}{\sigma_0}\right)^L y^{2L-1} e^{-\frac{Q_i^2 L}{\sigma_0} y^2} dy$$

$$f_Z(z) = \frac{1}{2\pi} \int_{-\infty}^{+\infty} G_Z(\omega) \exp(-j\omega z) d\omega. \quad (16)$$

Here, $G_Z(\omega)$ is the eigenfunction of Z ; ω is any real number and $j = \sqrt{-1}$.

On the basis of Equation (14), the PDF of the normalized version $\hat{Z} = Z/\sqrt{\sigma_0}$ of variable Z can be written as:

$$G_{\hat{Z}}(\omega) = \prod_{i=1}^N \int_{-\infty}^{+\infty} \frac{2e^{i\omega y}}{\Gamma(L)} (Q_i^2 L)^L y^{2L-1} e^{-Q_i^2 L y^2} dy \quad (17)$$

$$f_{\hat{Z}}(z) = \frac{1}{2\pi} \int_{-\infty}^{+\infty} G_{\hat{Z}}(\omega) \exp(-j\omega z) d\omega. \quad (18)$$

In a homogeneous area, $S = |Z_1 - Z_2|/\sqrt{\lambda_1 + \lambda_2}$, Z_1 and Z_2 are the weighted averages of N pixels within two contiguous homogeneous sub-areas, and λ_1 and λ_2 are the estimated scattering parameters of the two homogeneous sub-areas. Since the N pixels within homogeneous region are identically and independently distributed, Z_1 and Z_2 are identically and independently. Because usually the relation $Q_1 \neq Q_2 \neq \dots \neq Q_N$ holds, we cannot easily solve the analytical expressions of Equations (16) and (18). This means that we cannot obtain an analytical solution of the PDF for S . However, even though the analytical formulas of Equations (16) and (18) cannot be obtained, we can show that the PDF of S does not depend on the scattering coefficient σ_0 in homogeneous areas.

Since the values of λ_1 and λ_2 are proportional to the scattering coefficient σ_0 , $S = |Z_1 - Z_2|/\sqrt{\lambda_1 + \lambda_2}$ can be written in a convenient form as $S = |Z_1 - Z_2|/C\sqrt{\sigma_0}$, where

C is a positive constant. Consequently, the normalized versions $\hat{Z}_1 = Z_1/\sqrt{\lambda_1 + \lambda_2}$ and $\hat{Z}_2 = Z_2/\sqrt{\lambda_1 + \lambda_2}$ can be written as: $\hat{Z}_1 = Z_1/C\sqrt{\sigma_0}$ and $\hat{Z}_2 = Z_2/C\sqrt{\sigma_0}$, respectively. Because the PDFs of Z_1 and Z_2 are similar to Equation (16), their normalized versions \hat{Z}_1 and \hat{Z}_2 have similar PDFs as Equation (18), i.e., we have:

$$G_{\hat{Z}_1}(\omega) = \prod_{i=1}^N \int_{-\infty}^{+\infty} \frac{2e^{i\omega y}}{\Gamma(L)} (Q_i^2 C^2 L)^L y^{2L-1} e^{-Q_i^2 C^2 L y^2} dy \quad (19)$$

$$G_{\hat{Z}_2}(\omega) = \prod_{i=1}^N \int_{-\infty}^{+\infty} \frac{2e^{i\omega y}}{\Gamma(L)} (Q_i^2 C^2 L)^L y^{2L-1} e^{-Q_i^2 C^2 L y^2} dy \quad (20)$$

$$f_{\hat{Z}_1}(z_1) = \frac{1}{2\pi} \int_{-\infty}^{+\infty} G_{\hat{Z}_1}(\omega) \exp(-j\omega z_1) d\omega. \quad (21)$$

$$f_{\hat{Z}_2}(z_2) = \frac{1}{2\pi} \int_{-\infty}^{+\infty} G_{\hat{Z}_2}(\omega) \exp(-j\omega z_2) d\omega. \quad (22)$$

If \hat{Z}_1 and \hat{Z}_2 are independent variables, the PDF of the variable S can be given as:

$$f_S(s) = \begin{cases} \int_0^{+\infty} f_{\hat{Z}_1}(z_1) f_{\hat{Z}_2}(z_1 - s) dz_1 & \hat{z}_1 \geq \hat{z}_2 \\ \int_0^{+\infty} f_{\hat{Z}_1}(s + z_2) f_{\hat{Z}_2}(z_2) dz_2 & \hat{z}_1 < \hat{z}_2 \end{cases}. \quad (23)$$

It can be seen from Equations (21) to (23) that in a homogeneous area, $f_S(s)$ does not vary with the scattering coefficient σ_0 . This means that the UDR edge detector has the CFAR property for homogeneous areas.

The local weighted averages Z_1 and Z_2 are related to the scattering coefficient σ_0 and they are respectively proportional to the estimated scattering parameters λ_1 and λ_2 . If we replace λ_1 and λ_2 with Z_1 and Z_2 respectively, $S = |Z_1 - Z_2|/\sqrt{\lambda_1 + \lambda_2}$ can be written as $S = |Z_1 - Z_2|/\sqrt{Z_1 + Z_2} = |Z_1 - Z_2|/C\sqrt{\sigma_0}$, where C is a positive constant. Similarly to the analysis shown in Equations (21) to (23), we can easily deduce that the PDF of $S = |Z_1 - Z_2|/\sqrt{Z_1 + Z_2}$ does not vary with the scattering coefficient σ_0 . This implies that replacing λ_1 and λ_2 with Z_1 and Z_2 will not affect the CFAR property of the UDR edge detector.

According to the analysis shown in this sub-section, we find that the main purpose of the ratio operation is to achieve the CFAR property for the edge detector. For example, $S = |Z_1 - Z_2|/Z_1$ also has the CFAR property. But such a detector cannot guarantee the unbiased edge localization ability. The reason is described in the following subsection III.C.

C. Unbiased Edge Localization

The sudden jump of gray scales forms an ideal step edge. However, speckle noise and some other uncertain factors often make the abrupt changes of ideal step edges gradual and fuzzy. Edges in SAR images can be well modeled by the non-ideal edge model rather than the ideal one [37]. The difference of non-ideal edges from ideal ones is that the former contains a transition zone, while the latter does not. A transition zone is usually with several-pixel width consisting of a true edge pixel and several adjacent ones.

Let a , μ_1 and μ_2 ($\mu_1 < \mu_2$) represent three positive constants, and $I_E(x)$ be a 1D edge function without speckle. Assume that the real edge position of edge $I_E(x)$ is at $x = 0$. An ideal step edge is shown in Figure 2(a), where $I_E(x) = \mu_1$ for $x \leq 0$, and $I_E(x) = \mu_2$ for $x > 0$. A non-ideal edge is shown in Figure 2(b), where $I_E(x) = \mu_1$ for $x \leq -a$, and $I_E(x) = \mu_2$ for $x \geq a$. The area of $|x| < a$ is defined as the transition zone. Within the transition zone, the value of $I_E(x)$ is usually modeled as nonlinearly varying between μ_1 and μ_2 . For most cases, the size of the transition zone is very small.

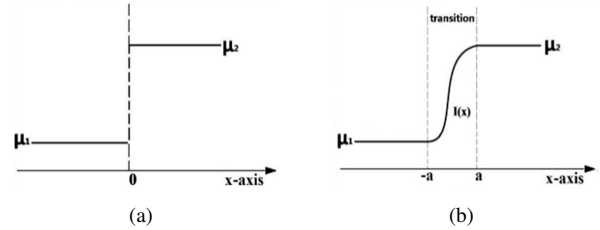


Fig. 2. Illustration of step edge models. (a) The ideal step edge model and (b) the nonideal step edge model.

The $h_{UDR}^{\parallel}(y)$ and the $h_{UDR}^{\perp}(x)$ combine to determine the performance the UDR, in which $h_{UDR}^{\parallel}(y)$ mainly controls the anti-noise property of the UDR, and $h_{UDR}^{\perp}(x)$ mainly determines the localization accuracy. When the UDR edge detector is shifted across a 2D edge, the edge position is set at the location where the edge strength achieves the maximum. For easier illustration, we use the case that $h_{UDR}^{\perp}(x)$ directly performs on a 1D edge to analyze the detection precision of the UDR.

The localization bias η is the difference between the real edge position (suppose the real edge position is at $x = 0$) and the expectation of the estimated edge position, denoted as \hat{x} , i.e., $\eta = \langle \hat{x} \rangle$ [24]. As shown in Figure 2, since $\mu_2 > \mu_1$, the estimated \hat{x} is evaluated by:

$$\begin{aligned} \hat{x} &= \arg \max_{x_0} S(x_0) = \max_{x_0} \left(\frac{|\bar{Z}(x_0) - \underline{Z}(x_0)|}{\sqrt{\bar{\lambda}(x_0) + \underline{\lambda}(x_0)}} \right) \\ &= \max_{x_0} \left(\frac{\bar{Z}(x_0) - \underline{Z}(x_0)}{\sqrt{\bar{\lambda}(x_0) + \underline{\lambda}(x_0)}} \right) \end{aligned} \quad (24)$$

Since $\bar{\lambda}(x_0)$ and $\underline{\lambda}(x_0)$ can be viewed as two pre-estimated constants, Equation (24) can simply be written as:

$$\hat{x} = \frac{1}{\sqrt{\bar{\lambda} + \underline{\lambda}}} \max_{x_0} (\bar{Z}(x_0) - \underline{Z}(x_0)) \quad (25)$$

If $I_E(x)$ is a 1D ideal edge function as shown in Figure 2(a), there evidently is $\eta = 0$. When $I_E(x)$ is a 1D non-ideal edge function as shown in Figure 2(b), for $x_0 \in [-a, a]$, $S(x_0)$ is computed by Equation (26). In this equation, $\int_0^{+\infty} h_{UDR}^{\perp}(x) dx = \int_{-\infty}^0 h_{UDR}^{\perp}(-x) dx = 1$ has been exploited.

It can be seen from Equation (6) that $h_{UDR}^{\perp}(x)$ only has a single peak. The location of the peak, denoted as \tilde{x} , is determined by the adjustable parameters of $h_{UDR}^{\perp}(x)$. In the presence of speckle, most of step edges in SAR images are

$$\begin{aligned}
S(x_0) &= \frac{\bar{Z}(x_0) - \underline{Z}(x_0)}{\sqrt{\bar{\lambda} + \underline{\lambda}}} = \frac{1}{\sqrt{\bar{\lambda} + \underline{\lambda}}} [I_E(x_0) \otimes h_{UDR}^\perp(x) - I_E(x_0) \otimes h_{UDR}^\perp(-x)] \\
&= \frac{1}{\sqrt{\bar{\lambda} + \underline{\lambda}}} \left[\int_0^{+\infty} I_E(x_0 + x) h_{UDR}^\perp(x) dx - \int_{-\infty}^0 I_E(x_0 + x) h_{UDR}^\perp(-x) dx \right] \\
&= \frac{1}{\sqrt{\bar{\lambda} + \underline{\lambda}}} \left[\int_{a-x_0}^{+\infty} h_{UDR}^\perp(x) \mu_2 dx + \int_0^{a-x_0} h_{UDR}^\perp(x) I_E(x_0 + x) dx \right. \\
&\quad \left. - \int_{-\infty}^{-x_0-a} h_{UDR}^\perp(-x) \mu_1 dx - \int_{-x_0-a}^0 h_{UDR}^\perp(-x) I_E(x_0 + x) dx \right] \tag{26} \\
&= \frac{1}{\sqrt{\bar{\lambda} + \underline{\lambda}}} \left[\int_0^{+\infty} h_{UDR}^\perp(x) \mu_2 dx + \int_0^{a-x_0} h_{UDR}^\perp(x) (I_E(x_0 + x) - \mu_2) dx \right. \\
&\quad \left. - \int_{-\infty}^0 h_{UDR}^\perp(-x) \mu_1 dx - \int_{-x_0-a}^0 h_{UDR}^\perp(-x) (I_E(x_0 + x) - \mu_1) dx \right] \\
&= \frac{\mu_2 - \mu_1}{\sqrt{\bar{\lambda} + \underline{\lambda}}} + \frac{1}{\sqrt{\bar{\lambda} + \underline{\lambda}}} \left[\int_0^{a-x_0} h_{UDR}^\perp(x) (I_E(x_0 + x) - \mu_2) dx - \int_{-x_0-a}^0 h_{UDR}^\perp(-x) (I_E(x_0 + x) - \mu_1) dx \right]
\end{aligned}$$

non-ideal ones with small transition zone. Hence, for most non-ideal step edges, we can maintain $a < \tilde{x}$ at most of time, which means that $h_{UDR}^\perp(|x|)$ makes pixels near $I_E(x_0)$ have relatively small weights. Since $I_E(-a)/\mu_1 - 1 = 0$ and $I_E(a)/\mu_2 - 1 = 0$, setting the differential of $S(x_0)$ with respect to x_0 to zero and ignoring the second and higher order yields Equation (27). Since the filter $h_{UDR}^\perp(|x|)$ is symmetrical, by exchanging the upper bound of the integrator shown in this equation, $h_{UDR}^\perp(-x)$ is changed as $h_{UDR}^\perp(x)$.

Because of the coherent nature of the illumination, SAR images are speckled. Let $I_N(x)$ be a 1D non-ideal step edge with speckle noise. According to the multiplicative noise model, we can safely assuming $\partial I_N(x_0)/\partial x_0 = \partial I_E(x_0)\zeta(x_0)/\partial x_0 = (\mu_2 - \mu_1)\zeta(x_0)/2a$ for $x_0 \in [-a, a]$, where $\zeta(\bullet)$ is multiplicative noise with unit mean. Then, Equation (27) can be rewritten as Equation (28).

Since $\mu_2 \neq \mu_1$, it can be seen from Equation (28) that we must have:

$$\int_0^{a-x_0} h_{UDR}^\perp(x) \zeta(x_0+x) dx = \int_0^{x_0+a} h_{UDR}^\perp(x) \zeta(x_0-x) dx \tag{29}$$

In order to keep the above equality, the length of integrating interval $[0, a+x_0]$ must be equal to that of the integrating interval $[0, a-x_0]$ in most instances or in the statistical sense. Hence, the equality in (29) must satisfy $E\{a+x_0\} = E\{a-x_0\}$ or $\eta = E\{x_0\} = 0$. It means the edge position estimated by $h_{UDR}^\perp(|x|)$ is statistical unbiased. Since an approximation has been used in the proof of the unbiasedness, the proposed UDR is not a strict unbiased detector. Hence, the word of unbiased in this paper technically refers to approximate unbiased.

Process and result of deriving are illuminated that the unbiased property of the UDR is entirely unrelated to the value of $1/\sqrt{\bar{\lambda} + \underline{\lambda}}$. Consequently, a direct substitution of \bar{Z} and \underline{Z} for $\bar{\lambda}$ and $\underline{\lambda}$ will not affect the unbiased property of the UDR. In Appendix A, we briefly explain the reason why traditional ratio-based edge detectors are biased for nonideal step edges.

UDR can work under the influence of the transition zone. Hence, we believe that UDR is also applied to ramp edges with small ramp width.

From the mentioned theoretical derivation, we can see that the unbiased property of UDR is not only attributed to the difference operation, but also related to the shape of $h_{UDR}^\perp(|x|)$. Because during the derivation, we use a reasonable assumption that $h_{UDR}^\perp(|x|)$ can make the pixels near $I_E(x_0)$ have relatively small weights. For a detector adopting the difference operation, like Canny detector, it cannot show unbiased property if it does not comply with the assumption. Interestingly, if a function has the similar shape with $h_{UDR}^\perp(|x|)$, it can replace the vertical filter of UDR, but do not harm the unbiased property. For example, the power-modulated-gaussian (PMG) function $h_{PMG}(|x|) = |x|^\alpha \exp(-x^2/\beta^2)$ can be used as a substitute for $h_{UDR}^\perp(|x|)$. We perform PMG and $h_{UDR}^\perp(|x|)$ on several SAR images including simulated and real-world ones. Experiments prove that $h_{PMG}(|x|)$ has the similar detection performance as $h_{UDR}^\perp(|x|)$. In this paper, $h_{UDR}^\perp(|x|)$ is adopted because it is more common and its computational complexity is slightly lower than $h_{PMG}(|x|)$.

D. Simplified UDR

According to the analysis shown in the Sub-sections III.2 and III.3, we know that it is completely safe to directly substitute the local weighted averages for the estimated scattering parameters. That is to say, $\bar{Z}_{UDR}(x, y)$ and $\underline{Z}_{UDR}(x, y)$ can be used to replace $\bar{\lambda}(x, y)$ and $\underline{\lambda}(x, y)$, respectively. After substituting, Equation (9) is written as:

$$\check{S}_{UDR}(x, y) = \frac{|\bar{Z}_{UDR}(x, y) - \underline{Z}_{UDR}(x, y)|}{\sqrt{\bar{Z}_{UDR}(x, y) + \underline{Z}_{UDR}(x, y)}} \tag{30}$$

Similarly, we can use $\bar{Z}_{UDR}^\theta(x, y)$ and $\underline{Z}_{UDR}^\theta(x, y)$ to replace $\bar{\lambda}^\theta(x, y)$ and $\underline{\lambda}^\theta(x, y)$, respectively. After substituting, Equation (11) becomes:

$$\begin{aligned}
0 &= \frac{1}{\sqrt{\bar{\lambda} + \underline{\lambda}}} \left[\int_0^{a-x_0} h_{UDR}^\perp(x) \frac{\partial I_E(x_0+x)}{\partial x_0} dx - \int_{-x_0-a}^0 h_{UDR}^\perp(-x) \frac{\partial I_E(x_0+x)}{\partial x_0} dx \right] \\
&= \int_0^{a-x_0} h_{UDR}^\perp(x) \frac{\partial I_E(x_0+x)}{\partial x_0} dx - \int_0^{x_0+a} h_{UDR}^\perp(x) \frac{\partial I_E(x_0-x)}{\partial x_0} dx
\end{aligned} \tag{27}$$

$$\begin{aligned}
0 &= \int_0^{a-x_0} h_{UDR}^\perp(x) \frac{\mu_2 - \mu_1}{2a} \zeta(x_0+x) dx - \int_0^{x_0+a} h_{UDR}^\perp(x) \frac{\mu_2 - \mu_1}{2a} \zeta(x_0-x) dx \\
&= \frac{\mu_2 - \mu_1}{2a} \left[\int_0^{a-x_0} h_{UDR}^\perp(x) \zeta(x_0+x) dx - \int_0^{x_0+a} h_{UDR}^\perp(x) \zeta(x_0-x) dx \right]
\end{aligned} \tag{28}$$

$$\check{S}_{UDR}^\theta(x, y) = \frac{|\bar{Z}_{UDR}^\theta(x, y) - \underline{Z}_{UDR}^\theta(x, y)|}{\sqrt{\bar{Z}_{UDR}^\theta(x, y) + \underline{Z}_{UDR}^\theta(x, y)}} \tag{31}$$

The ESM and EDM computed by Equation (31) are as follows.

$$E\check{S}M_{UDR}(x, y) = \max_{k=0,1,\dots,M-1} \check{S}_{UDR}^{\theta_k}(x, y), \tag{32}$$

$$E\check{D}M_{UDR}(x, y) = \arg \max_{\theta_k} \check{S}_{UDR}^{\theta_k}(x, y) + \pi/2, \tag{33}$$

where $\theta_k = k\pi/M$ and M are the number of orientations. The variable $k = 0, 1, \dots, M-1$ is the index of orientation. According to Equations (32) and (33), we perform the NSHT operation on the obtained $E\check{S}M_{UDR}(x, y)$ and $E\check{D}M_{UDR}(x, y)$, which produces the binary edge map of the image $I(x, y)$.

The aforementioned theoretic analysis shows that substituting the local weighted averages for the estimated scattering parameters will not affect the performance of the UDR. This simplified version of the UDR does not need to compute the estimated scattering parameters, $\bar{\lambda}(x, y)$ and $\underline{\lambda}(x, y)$, and hence, can effectively save the computation time. For simplicity, the simplified version of the UDR is recorded as S-UDR.

E. Computational Complexity Analysis

For S-UDR, its calculated amount is mainly from the convolution operation. Suppose the edge detection filter $h_{UDR}(x, y)$ is rotated to P different directions. The filter and its rotated versions are all truncated to the size of $(2W+1) \times (2W+1)$. The computational complexity of S-UDR is nearly equal to $O(PM^2(2W+1)^2)$ for dealing with an $M \times M$ SAR image. For most of existing popular ratio-based SAR edge detectors, like ROA, GGS and RBED et al., their computational complexities are of the order of magnitude of $O(N^5)$ [17]. That means, the S-UDR has almost the same computational complexity with the ratio-based detectors. As for UDR, its computational amount includes the convolution operation and the estimation of parameter λ . Hence, the computational complexity of UDR is higher than ratio-based detectors and its simplified version.

IV. EXPERIMENTAL RESULTS

In this section, we compare the proposed edge detector UDR with existing popular edge detectors including Canny edge detector [12], the ROA [14], the ROEWA [15], the GGS [16], and RBED [17]. The compared detectors used different detection filters, but all adopted the same NSHT post-processing method. The detection filter of the UDR, denoted as $h_{UDR}(x, y)$, is shown in Equation (8). The detection filters of ROA $h_{ROA}(x, y)$, ROEWA $h_{ROEWA}(x, y)$, GGS $h_{GGS}(x, y)$ and RBED $h_{RBED}(x, y)$ are written as:

$$\begin{cases} h_{ROA}(x, y) = h_{MF}^\perp(|x|)h_{MF}^\parallel(y) \\ h_{MF}^\perp(x) = \begin{cases} 1/w_{MF} & 0 < |x| \leq w_{MF}, w_{MF} > 0 \\ 0 & \text{else} \end{cases} \\ h_{MF}^\parallel(y) = \begin{cases} 1/l_{MF} & |y| \leq l_{MF}, l_{MF} > 0 \\ 0 & \text{else} \end{cases} \end{cases} \tag{34}$$

$$\begin{cases} h_{ROEWA}(x, y) = h_{ROEWA}^\perp(|x|)h_{Gaussian}^\parallel(y) \\ h_{ROEWA}^\perp(|x|) = \exp(-\varsigma_{ROEWA}|x|) \\ h_{Gaussian}^\parallel(y) = \exp(-y^2/2\sigma_{ROEWA}^2) \\ \varsigma_{ROEWA} > 0, \sigma_{ROEWA} > 1 \end{cases} \tag{35}$$

$$\begin{cases} h_{GGS}(x, y) = h_{GGS}^\perp(|x|)h_{Gaussian}^\parallel(y) \\ h_{GGS}^\perp(|x|) = |x|^{\alpha_{GGS}-1} \exp(-|x|/\beta_{GGS}) \\ h_{Gaussian}^\parallel(y) = \exp(-y^2/2\sigma_{GGS}^2) \\ \alpha_{GGS} > 1, \beta_{GGS} > 0, \sigma_{GGS} > 1 \end{cases} \tag{36}$$

$$\begin{cases} h_{RBED}(x, y) = h_{RBED}^\perp(|x|)h_{RBED}^\parallel(y) \\ h_{RBED}^\perp(|x|) = |x|^{\alpha_{RBED}} \exp(-|x|^2/\beta_{RBED}^2) \\ h_{RBED}^\parallel(y) = \begin{cases} 1 & |y| \leq l_{RBED} \\ \exp\left(\frac{-(|y|-l_{RBED})^2}{2\sigma_{RBED}^2}\right) & |y| > l_{RBED} \end{cases} \\ \alpha_{RBED} > 0, \beta_{RBED} \neq 0, l_{RBED} \geq 0, \sigma_{RBED} > 1 \end{cases} \tag{37}$$

The parallel filter of RBED is the same as that of UDR, since literature [17] indicates that the flat bell-shaped function can sufficiently exploit the information of multiple adjacent edge-pixels to decrease false positive detection rate. Unless specially emphasized, all compared detectors keep the same effective support area. Moreover, all of the experimental results

presented in this paper are obtained on a computer with an Intel Core (TM) i5 CPU of 3.2 GHz and 4GB RAM. The operating system is Windows 7. We use MATLAB (R2016a) for programming.

A. The Impact of the Size of the Transition Zone on Localization Accuracy

First, the impact of the size of the transition zone on localization accuracy is discussed. For easier discussion, let us denote the edge contrast and the size of transition zone as ρ and $2a$, respectively. Edge contrast means the reflectivity ratio between two adjacent homogeneous areas separated by the edge. Figure 3 shows three non-ideal edge images and their corresponding ones with two-look amplitude-format contaminated with speckle noise. The contrasts of the three non-ideal edges are $\rho = 10$. Since small contrast will largely affect the detection performance of a detector (as we will see), a big contrast value $\rho = 10$ is used. The transition zones of the three simulated non-ideal edges are 2-pixel width, 4-pixel width and 6-pixel width respectively. The profiles of simulated non-ideal edges without speckle noise are plotted and embedded in the Figure 3(a). Figures 3(b) to (d) show the detection results.

In each sub-figure, from left to right, the edges are obtained using the detectors of UDR, Canny, ROA, ROEWA, GGS, and RBED. In these figures, we use blue dash lines to indicate the ground-truth location of the non-ideal edges. Considering that the real edge pixel is sub-pixel level, we accept the closest pixel on either side of the sub-pixel as a correct edge pixel.

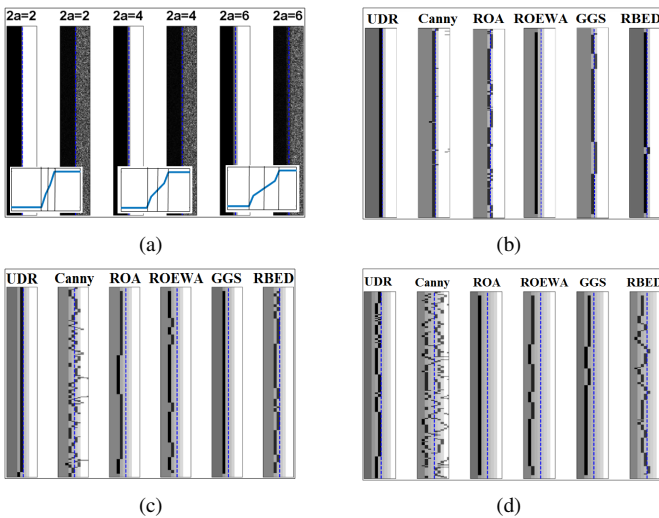


Fig. 3. Comparison of edges detected with different edge detectors showing the impact of the transition zones of various sizes on localization accuracy. (a) Three non-ideal edges with the same edge contrast ($\rho = 10$) and different transition zones and their corresponding two-look amplitude-format speckled ones. The sizes of the transition zone ($2a$) of the three edges are 2-pixel width, 4-pixel width and 6-pixel width respectively. (b), (c) and (d) are the edge detection results obtained with the compared detectors, i.e., UDR, Canny, ROA, ROEWA, GGS, and RBED, on non-ideal edges with $2a = 2$, $2a = 4$, $2a = 6$, respectively.

Next, we discuss the performances of compared detectors on different sizes of transition zones.

- 1) When $2a = 2$, ROA and GGS correctly locates the positions of all edge pixels. However, they show a

fluctuant line that is formed by several edge-pixels with various locations. The fluctuant degree of GGS is smaller than that of ROA. The bias of ROEWA is one pixel and toward to the darker side. As for RBED, UDR and Canny, they achieve satisfactory localization results.

- 2) When $2a = 4$, only UDR shows unbiased result. The detection result and the fluctuant phenomenon of Canny go worse obviously. Because Canny has no CFAR. ROA, ROEWA, GGS and RBED show bias results. The bias of GGS is 1-pixel width, while the bias of ROA is slightly bigger than 1-pixel width. Among ROA, ROEWA, GGS and RBED, ROEWA has the biggest value of bias. The bias of ROEWA is almost equal to 2-pixel width. Most edge-pixels are correctly localized by RBED, while parts of them are bias. Hence, the average bias of RBED is slightly smaller than 1-pixel width.
- 3) When $2a = 6$, the biases of ROA, ROEWA, GGS and RBED are further increased. Among these detectors, only RBED can correctly detect a minority of edge-pixels. The bias of GGS is smaller than ROA, and the bias of ROA is smaller than ROEWA. Canny operator outputs two responses for a single edge. This means speckle and transition zone size easily affect the localization performance of Canny. From Figure 3(d), we can see that GGS has better vision effect than UDR, since the edges of GGS are with a smoother degree than UDR. In this case, UDR declares part of biased edge-pixels, while all edge-pixels declared by GGS are bias. The bias degree of GGS is much larger than that of UDR. Clearly, subjective evaluation result sometimes is totally opposite to objective evaluation. Hence, from the aspect of location bias, UDR is better than GGS. From the aspect of smooth degree, GGS is better than UDR when $2a = 6$. When $2a$ is smaller than 6-pixel width, the smooth degree of UDR is better than that of GGS.

In this experiment, our UDR shows the smallest bias, followed by RBED, GGS, ROA, ROEWA, and Canny. With the increase of the size of the transition zone, it will be increasingly hard to accurately localize the edge position. Hence, the biases of compared detectors increase as the transition zone increases. The reason why ROEWA always shows the biggest bias is because the vertical filter of ROEWA always gives the biggest weights to the pixels in the transition zone [17]. Among all compared detectors, our UDR edge detector has good localization ability for all sizes of transition zone. More importantly, our proposed UDR can show stable and smooth lines when transition zone is not too big.

Unlike other detectors, UDR, theoretically, is an unbiased edge detector. The biased edge pixels declared by UDR are caused by two reasons. One is random noise. The other one is the size of the transition zone. With the size of the transition zone increases, the assumption that the size of the transition zone is small is difficult to keep valid. Hence, we can see that the number of biased edge pixels reported by UDR grows more as the transition zone size increases.

As for other compared detectors, they theoretically are bias. The theoretical derivation indicates that the unbiased property is not only related to the difference operation, but also

impacted by the shape of the detector. For example, the shape of Canny does not follow our requirement. While RBED does not adopt the difference operation. Hence, they theoretically are bias, which is supported by the experimental results.

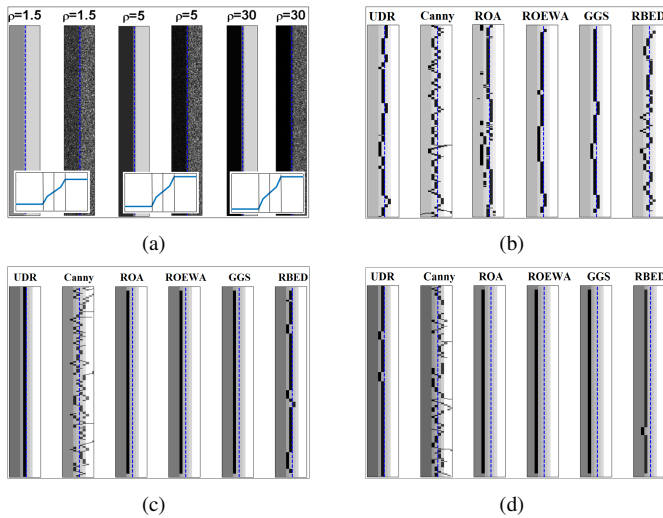


Fig. 4. Comparison of edges detected with different edge detectors showing the impact of edge contrast ρ on localization accuracy. (a) shows three non-ideal edges with different contrasts and their corresponding two-look amplitude-format speckled ones. The size of the transition zones of the three edges are 4-pixel. The contrasts (ρ) of the three edges are $\rho = 1.5$, $\rho = 5$, and $\rho = 30$ respectively. (b), (c) and (d) are the results of compared detectors (UDR, Canny, ROA, ROEWA, GGS, and RBED) on $\rho = 1.5$, $\rho = 5$, and $\rho = 30$, respectively.

B. The Influence of Edge Contrast on Localization Accuracy

The influence of edge contrast ρ on localization accuracy is discussed. In this experiment, the size of transition zone is fixed as $2a = 4$. Figure 4(a) includes three non-ideal edges and their contrasts are $\rho = 1.5$, $\rho = 5$, and $\rho = 30$ respectively. The profiles of simulated non-ideal edges without speckle noise are plotted and embedded in the Figure 4(a). Figures 4(b) to (d) show the detection results of the compared detectors.

- 1) By carefully observing Figure 4(b), we find that when $\rho = 1.5$, all detectors are unbiased. However, since the contrast is small, some false edges are easily detected, in which Canny, and ROA detect more false edges. Edges with small contrasts are usually more difficult to be detected than edges with big contrasts because speckle noise has more impact on small contrasts edges. Hence, for edges with a small contrast, detectors usually pay more attention to ‘find’ the edge rather than ‘localize’ the edge. In this sense, detectors GGS and UDR show better results. UDR declares 13 biased edge-pixels, while GGS declares 10 biased edge pixels. The result is considered to have involved randomly noise. Since the edge of GGS has a better smooth degree, GGS shows far better detection result than UDR visually. But from the aspect of location bias, the two detectors are similar in performance. As the contrast increases, the focus of our attention is still the localization ability of detector.
- 2) When $\rho = 5$, the biases of ROA, ROEWA and GGS are 1-pixel width. Consider Figure 4(b), when ROA,

ROEWA, and GGS perform on the edge with $\rho = 1.5$, their biases disappear; when they perform on the edge with $\rho = 5$, the vanished biased appear again. That is to say, the detection results of ROA, ROEWA, and GGS are sensitive to the changes of edge contrast.

- 3) When $\rho = 30$, the biases of ROA, ROEWA and GGS further increases and reach 2-pixel width. In this case, the bias of RBED is approximately equal to 1-pixel width and the bias is towards the darker side. When RBED is run on the edge with a small contrast, its detection result will show violent fluctuation phenomena. However, as the contrast becomes bigger, the variances of fluctuation of RBED become smaller and smaller.

Putting this all together, we can see that with the contrast increasing, the biases of ROA, ROEWA, RBED and GGS become larger, in which the degree of bias change of RBED is the smallest. Due to the impact of the speckle noise, the detection result of Canny is unsatisfactory. The UDR shows unbiased results for $\rho = 1.5$, $\rho = 5$, and $\rho = 30$. This indicates that the localization ability of the UDR is not sensitive to the changes of contrast.

C. Edge Detection Results on Simulated SAR Images

Let us use several simulated SAR images to compare the detectors UDR, GGS, RBED, ROEWA and ROA. Since Canny is incapable in SAR images, it is no longer included in the following comparisons. This subsection includes three experiments. The first one evaluate the detectors by the subjective-visual method. The other two experiments analyze the detectors by objective and quantitative evaluation indexes.

Figure 5(a) shows an amplitude SAR image with 507×474 pixels. The number of looks is three. In this simulated image, the effects of transition zone size and edge contrast on detection performance are combined, which clearly increases the difficulty of detection. We run the compared detectors on the image shown in Figure 5(a) separately. For a fair comparison, the low and high thresholds of the compared detectors are tuned such that their binary edge maps contain comparable number of correctly detected edge pixels. The binary edge maps are shown in Figures 5(b)-(f) respectively.

First, we compare the detectors from the aspect of false edges. The proposed UDR shows a satisfactory result, although it misses a few edges and reports a small number of false edge pixels. For example, UDR detects a non-smooth edge at the top-middle of the image. The contrast of this edge is only 1.26, but its transition zone is nearly equal to 5-pixel width. From Figure 5(f) we can clearly see that the ROA approach shows the most false edge pixels. This is because the detection filter of ROA has very high first side lobe. A high side lobe results in many un-wanted high frequency components being leaked. These leaked high frequency components are often wrongly declared as edge pixels. Because of the good smooth performance of the parallel filters, RBED, GGS and ROEWA show less false edge-pixels than ROA.

Second, we compare the detectors from the angle of localization precision. We can see that, impacted by the transition zone, the edge positions obtained with ROA, GGS, ROEWA

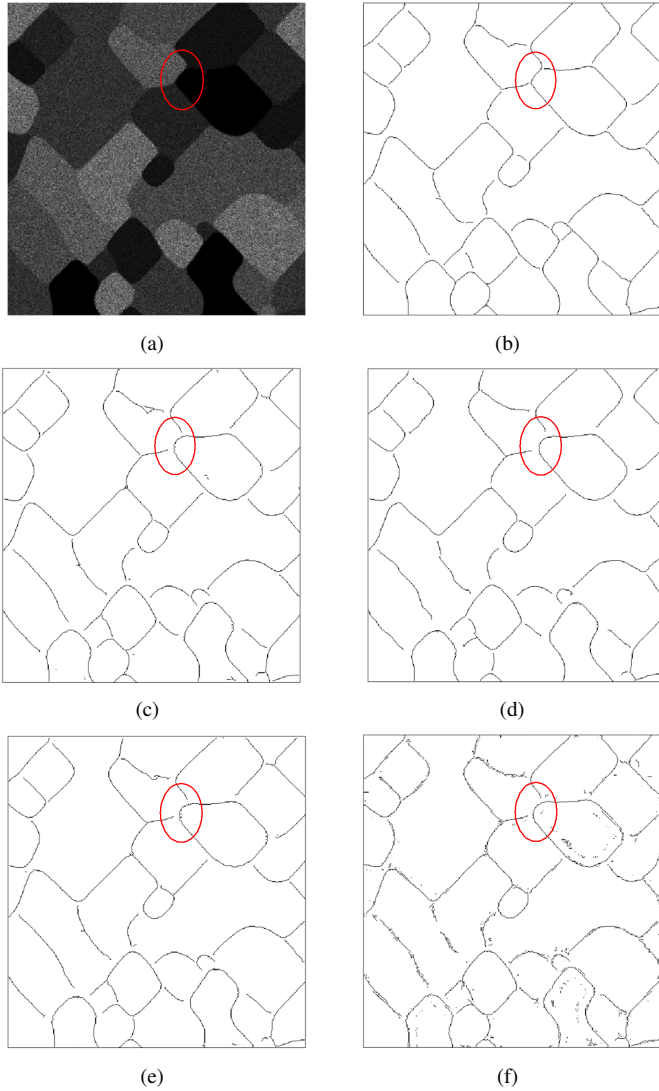


Fig. 5. Edge binary maps obtained by using ROA, ROEWA, GGS, and RBED on the three-look amplitude-format SAR image. (a) Simulated SAR image. Edge binary maps of (b) UDR, (c) GGS, (d) RBED, (e) ROEWA, and (f) ROA.

and RBED show visible bias, while our UDR can accurately detect the position of the majority of edges. Biased edges lead to obvious distorted boundaries. Hence, for other detectors, the detected edges are shorter than that of UDR. Take the boundaries of a dark region marked by red circle marker as an example. In Figures 5(c)-(f), the boundaries of this region bend towards the interior of the region.

In the following, some objective evaluation metrics are used to compare the detection performances of UDR, ROA, ROEWA, GGS, and RBED. Pratt's figure of merit [38][39], which has been widely used to evaluate the localization precision, is used first as an objective evaluation indicator.

In the evaluation of the Pratt's figure of merit, the testing image must have a standard edge map with known edge position. The standard edge map consists of edge region and non-edge region. With the standard edge map, the value of Pratt's figure of merit of a given binary edge map is uniquely

computed by

$$P = \frac{1}{\max(N_{ID}, N_{DE})} \sum_{i=1}^{N_{DE}} \frac{1}{1 + \kappa d_i^2} \quad (38)$$

where N_{ID} and N_{DE} are the numbers of ideal edge-pixels and detected edge-pixels, respectively. An ideal edge-pixel means the pixel located in the edge region. Let us use κ denote the penalization constant (in this paper we fix $\kappa = 2$ for a stronger penalization of biased edge-pixels), and d_i denote the distance between the i -th detected edge-pixel and the closest ideal edge-pixel. The value of Pratt's figure of merit is known as P score. According to Equation (38), we know that the higher P score the detector gets, the better localization ability the detector has. Further details concerning Pratt's figure of merit can be found in literature [37][38].

Figure 6 shows a 127×151 simulated image and its corresponding standard edge map. The edges in Figure 6(a) have different transition zone sizes and different edge contrasts. With the scene in Figure 6(a), a series of images with different number of looks are simulated. The number of looks varies from one to nine. The P scores of the compared detectors are separately computed on each simulated SAR image.

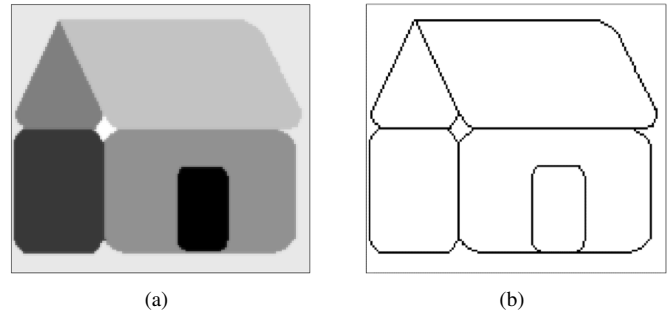


Fig. 6. Simulated images for Pratt's figure of merit. (a) Simulated image with different transition zone sizes and different contrasts. (b) Standard edge map of (a).

We evaluate the P scores of the compared detectors when they get their individual optimal parameter setting. We give a parameter space for each compared detector and the parameter setting of a detector is taken from its parameter space. For each parameter setting, the P score is computed. Only the highest value of P score is recorded. The use of parameter space avoids the effect of the parameter settings on evaluating the performances of different detectors. In order to avoid the effect of the discrete parameter space and randomly speckle on P -score values of different detectors, we adopt the Monte Carlo approach. We repeat the independent trials 1000 times. The average result is recorded as the final P score.

The parameter space of ROA is:

$$\begin{cases} w_{MF} = \{3, 5, 7, 9, 11\} \\ l_{MF} = \{3, 5, 7, 9, 11\} \\ T_{low} = 0.05 + 0.05k_1, & k_1 = 0, 2, \dots, 10 \\ T_{high} = T_{low} + 0.05k_2, & k_2 = 0, 2, \dots, (0.6 - T_{low})/0.05 \end{cases}, \quad (39)$$

where T_{low} and T_{high} are the two public parameters involved in NSHT. Detectors DUR, GGS, RBED and ROEWA take T_{low} and T_{high} from Equation (39).

The parameter space of ROEWA is

$$\begin{cases} \sigma_{ROEWA} = 1/k_1, & k_1 = 1, 2, \dots, 15 \\ \sigma_{ROEWA} = 2 + 0.5k_2, & k_2 = 0, 1, \dots, 14 \end{cases} \quad (40)$$

The parameter space of GGS is

$$\begin{cases} \alpha_{GGS} = \{2, 3, 4, 5\} \\ \beta_{GGS} = 0.5 + 0.5k_1, & k_1 = 0, 1, \dots, 9 \\ \sigma_{GGS} = 2 + 0.5k_2, & k_2 = 0, 1, \dots, 14 \end{cases} \quad (41)$$

The parameter space of RBED is

$$\begin{cases} \alpha_{RBED} = \{2, 3, 4, 5\} \\ \beta_{RBED} = 2 + 0.5k_1, & k_1 = 0, 1, \dots, 14 \\ l_{RBED} = 2 + 0.5k_2, & k_2 = 0, 1, \dots, 4 \\ \sigma_{RBED} = 1.5 + 0.5k_3, & k_3 = 0, 1, \dots, 13 \end{cases} \quad (42)$$

The parameter space of UDR and S-UDR is

$$\begin{cases} \alpha = \{2, 3, 4, 5\} \\ \beta = 0.5 + 0.5k_1, & k_1 = 0, 1, \dots, 9 \\ l_{||} = 1 + k_2, & k_2 = 0, 1, \dots, 4 \\ \sigma_{||} = 1.5 + 0.5k_3, & k_3 = 0, 1, \dots, 13 \end{cases} \quad (43)$$

During the following experiment, all possible combinations of parameters within the parameter space are tried for the best results of each detector. In objective evaluation, we compare detectors at their individual optimal parameter setting, rather than at the same parameter setting. Hence, we do not restrict that the compared detectors should share the same parameter spaces. Over-expanding the given parameter spaces cannot further enlarge the values of P scores. Hence, we believe the given parameter space is a reasonable choice.

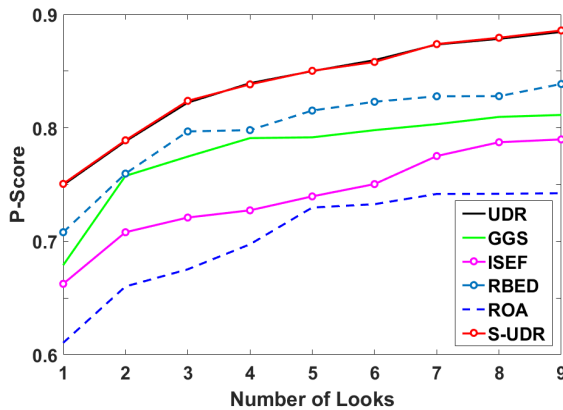


Fig. 7. Pratt's figure of merit for detectors UDR, simplified UDR (S-UDR), GGS, RBED, ROEWA and ROA with varying number of looks and varying parameter settings.

Figure 7 shows the curves of P score varying with number of looks. For further proof that S-UDR is equivalent to UDR, the P -score curve of S-UDR has also shown in Figure 7. We can see that, with the number of looks increasing, the P score

of each detector rises continuously. Take ROA as example. When ROA is used for single look SAR image, its P score is only 0.61; when the number of looks is nine, the P score of ROA is 0.74. The increase scope achieves nearly 0.13. Actually, the increases scopes of all compared detectors are above 0.12. This is because the larger the look number is, the weaker the influence of the speckle has. Consequently, it becomes easier to detect edges. Under all numbers of looks, our UDR always achieves the highest P score among all compared detectors. When the number of looks is equal to nine, the P score of our UDR even achieves 0.88. That means, UDR has the best localization accuracy among all compared detectors. According to Figure 7, RBED has better localization ability than GGS followed by ROEWA and ROA.

Equation (38) shows that false edge-pixels will pull down the P score of the detector. Hence, although ROA has better localization ability than ROEWA (please see the analysis of the first and the second experiment results), the average P score of ROA is smaller than ROEWA. The reason is that ROA always declares lots of false edge-pixels. Furthermore, because the parallel filter of RBED has better smooth ability, although literature [17] indicates that the vertical filter of GGS and the vertical filter of RBED should have the similar localization ability, the P score of GGS is lower than that of RBED.

On the other hand, we have noted that for a single-look SAR image, the P score of UDR is 0.75, while the P scores of other detectors are no more than 0.71. That means, UDR has a good localization accuracy under the influence of speckle. On the other hand, with decreasing number of looks, the P scores of UDR descend smoothly and have no obvious fluctuations. For GGS, ROA and ROEWA, when the number of looks decreases from 2 to 1, their P scores fall sharply. Steady P scores mean the localization ability of UDR is stable to the influence of speckle. Hence, we argue that UDR has a good anti-noise ability.

In this experiment, UDR and S-UDR show almost identical P -score values for the same number of looks. The fine differences between UDR and S-UDR are mainly from the effect of the discrete parameter space. At the present experimental conditions, the maximum deviation of P -score between UDR and S-UDR is 0.0015, the average deviation is about 0.0004 and the absolute average deviation is about 0.00087. Such differences can be further reduced or even eliminated by traversing all possible parameter settings. Hence, we believe UDR and S-UDR have the same localization precision.

Except for the localization precision, the false positive detection rate is another important criterion for evaluating detection performance. Hence, the receiver-operating-characteristic (ROC) curves [16], [40], [41] are used to objectively and fairly evaluate the false detection rate of different detectors. The ROC curves can evaluate the detection performance of different detectors at their individual best parameter settings and therefore avoid the effect of the parameter settings on evaluating the performances of different detectors.

Figure 8 shows a carton image and its corresponding ground truth edge map. The carton image has been used in literatures [16], [17]. It includes a lot of step edges with different transition sizes and different contrasts. The ground truth map

consists of edge region, non-edge region and match region, colored by black, grey and white, respectively. The match region is a tolerance of the edge region. Considering the influence of localization precision, we set the match region as a 3-pixel width tolerance of the edge region, which makes the ROC curves lenient. That is to say, we are lenient with the detectors that are not good at non-ideal edges detection or have poor localization abilities.

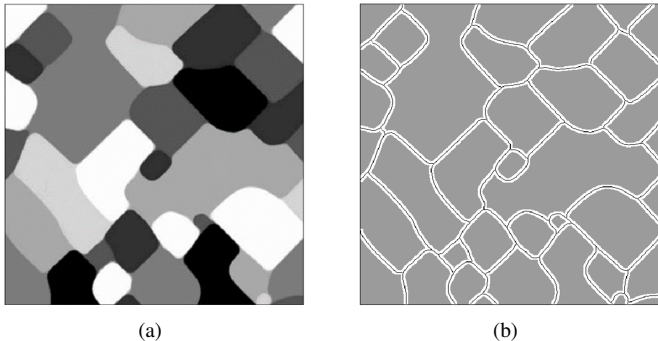


Fig. 8. (a) The cartoon image with step edges and (b) its ground truth edge map.

The pixels declared as edge-pixels but actually located in the non-edge region are counted as false edge-pixels; while the pixels declared as edge-pixels and located either in the match region or in the edge region are counted as true edge-pixels. For an ideal detector, it reports no false edge-pixels and correctly declares all edge-pixels at the same time. Hence, when a detector runs in its parameter space, the closer the ROC curve to the top-left corner, the better detection performance it will have. Since the obvious advantages of RBED over the ROA and ROEWA have already been analyzed by Wei. et al [17], the ROC curves of ROA and ROEWA are not plotted any more. The adjustable parameter spaces of GGS, RBED and UDR are chosen from Equations (40)-(42). As for the two common parameters T_{low} and T_{high} involved in the NSHT, they are taken from Equation (39).

For the scene in Figure 8(a), a three-look and a six-look SAR images are simulated. The ROC curves of GGS, RBED and UDR are shown in Figure 9. Figures 9 (a) and (b) are the ROC curves of three-look and six-look, respectively. For the three-look image, when the false positive rate is zero, the true positive rate of UDR can almost achieve 0.94. For the six-look image, the true positive rate of the proposed UDR is even up to nearly 0.96.

We believe the high true positive rate of our UDR mainly stems from its good localization ability. As for its low false positive rate is mainly because the parallel filter of UDR not only has good smooth ability but also can sufficiently exploit the information of multiple adjacent edge-pixels. Consequently, the false positive rate is lowered. The capability analysis of the parallel filter of UDR is described in details in literature [17]. Keep the same false positive rate, our UDR shows the highest true positive rate at most time. One exception is that, for the three-look image, when the false positive rate is between 0.011 to 0.016, the true positive rate of the UDR ($\alpha = 4$) is slightly lower than RBED ($\alpha = 2, 3$).

Several analyses to the results of ROC curves show that this exceptional conditions is caused by the random noise existing in SAR image.

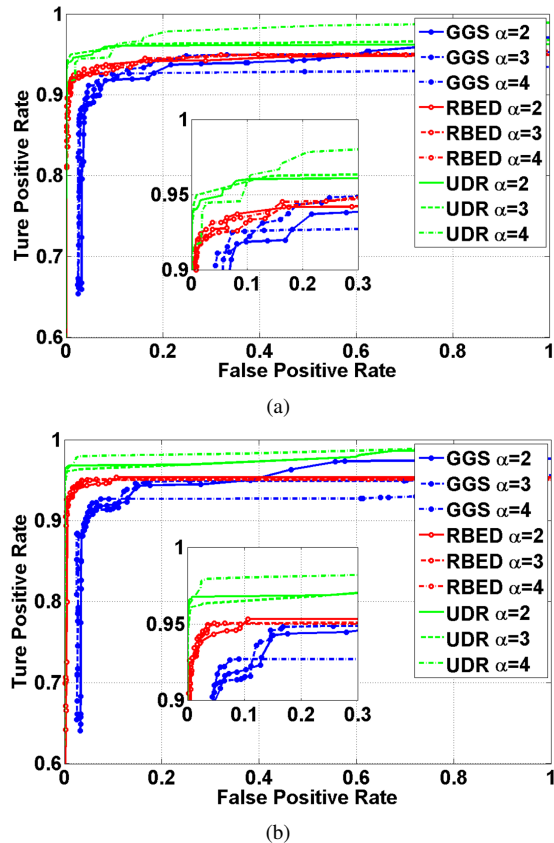


Fig. 9. ROC curves of GGS, RBED, and UDR for (a) three-look and (b) six-look SAR images.

D. Edge Detection Results on Real-world SAR Images

In this subsection, the detection results of the compared detectors on the real-world SAR image are shown. Detectors UDR and S-UDR firstly perform on a real-world image for proving they having identical performance. This real-world amplitude-format SAR image, shown in Figure 10(a), comes from the Rio Grande River near Albuquerque. It is downloaded from the website of Sandia National Laboratories. It has 432×552 pixels and its resolution is 1 meter. Detection results of UDR and S-UDR are shown in Figures 10(b) and (c). The two detectors nearly have the same visualization detection results. Figure 10(d) shows the XOR image of UDR and S-UDR. The same edges color in green while the different edges color in pink. We can see that the differences between two detectors are mainly in edge numbers. From the positions of detected edges, two detectors report the same result for the same edge pixel. The minor differences exist between the two detectors because the parameters are manually selected from a discrete parameter space. If their parameters change within a continuous parameter space, they will show the same binary edge maps. Theory and experiments have proved that UDR and S-UDR show the same detection ability. In the following experiments only the detection results of UDR are shown.

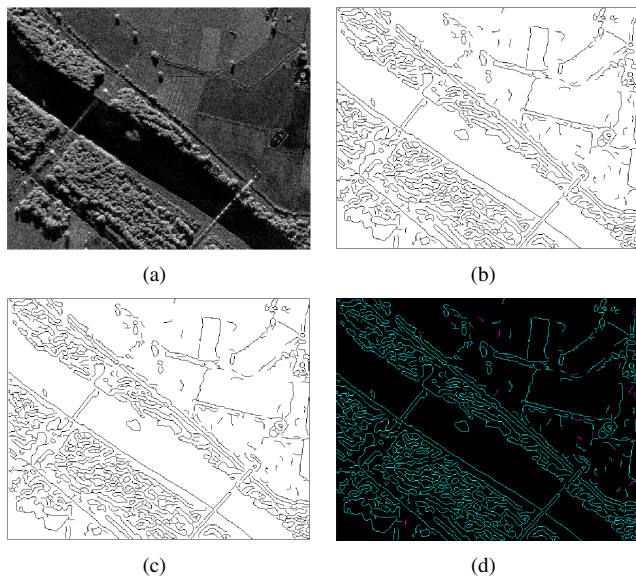


Fig. 10. Comparison of the binary edge maps obtained by UDR and S-UDR edge detectors on real world SAR images. (a) Amplitude-format of a real-world image with 1-m resolution from the Rio Grande River near Albuquerque. The binary edge maps obtained by (b) UDR and (c) S-UDR. (d) XOR image of (b) and (c). Edges in pink record the differences between UDR and S-UDR.

Figure 11(a) shows a 388×704 amplitude real-world image. It is obtained by TerraSAR-X SAR instrument with 3-m resolution. The image is of an agricultural scene near the Swabian Jura, Germany. Detectors perform on this real-world image to compare their detection ability on simple scene. The detection results are shown in Figure 11. Circles in Figure 11 mark several tiny structures. Clearly, UDR shows more accurate edge positions without obviously edge distortion. Rectangle marks a small dark region. For the sake of clarity, we zoom in this region. UDR shows clear and continuous region boundary. While the boundaries of this dark region declared by GGS, RBED, ROA and ROEWA are smaller than the original region area. The experimental results show that UDR has the best ability to locate edges in such agricultural SAR image.

Figure 12(a) shows a 396×472 amplitude real-world SAR image, which comes from the website of Sandia National Laboratories. It is a Ku-band SAR image of China Lake Airport in California (3-m resolution). Since the scene of the image is simple, the major edges are easily recognizable. Let us concern about some tiny edges. The ellipse markers shown in the image include two linear regions. The detection results show that none of the compared detectors can correctly detect the boundaries of the two linear regions, except for the proposed UDR. The GGS (Figure 12(c)) and RBED (Figure 12(d)) both report only one boundary. The ROEWA (Figure 12(e)) detects two boundaries, but the positions of the boundaries are moved. As for the ROA (Figure 12(f)), it is hard to identify the boundaries of the regions. This is because the ROA detects many false edge pixels, which mistakenly break and drown the regions boundaries. In addition, we can see that due to speckle noise, the detected edges of GGS, RBED, ROEWA and ROA are distorted to some extent, especially for

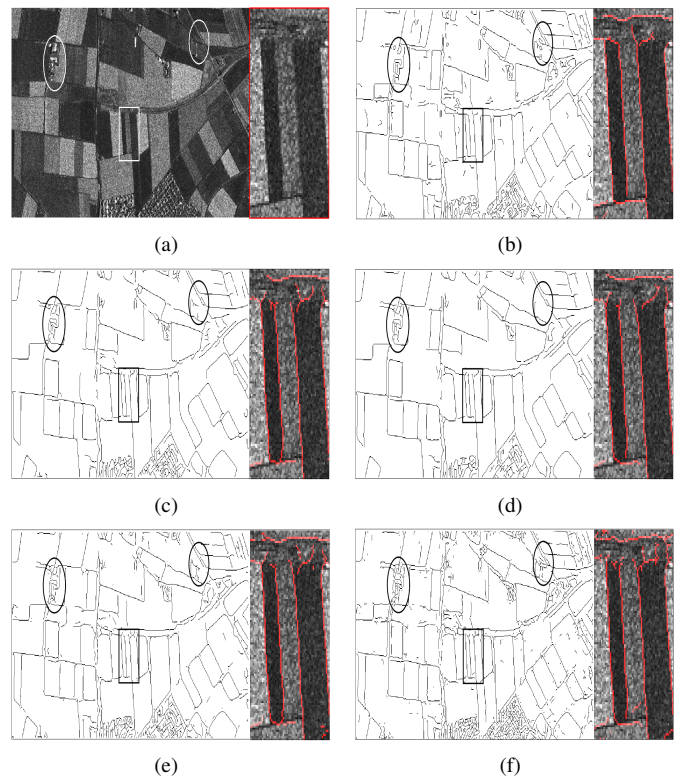


Fig. 11. Comparison of the binary edge maps on real world SAR image. (a) Amplitude-format of a real-world image obtained by TerraSAR-X SAR instrument on 1 July 2007. Agricultural scene with 3-m resolution near the Swabian Jura, Germany. The binary edge maps obtained with the edge detectors of (b) UDR, (c) GGS, (d) RBED, (e) ROEWA and (f) ROA.

GGS (Figure 12(c)) and ROEWA (Figure 12(e)), where there are noticeable distortions. This is because that both GGS and ROEWA take the Gaussian filter as their parallel filter. Under the same effective support area, the Gaussian filter results in stretched edges more easily. As for our UDR, the distortions in Figure 12(b) are almost invisible.

Then, the real-world amplitude-format SAR image with the same scene as Figure 10 are used to evaluate detectors performance on a nature scene. The detection results of compared detectors UDR, GGS, RBED, ROEWA and ROA are shown in Figure 13. UDR clearly shows most of boundaries. In the ellipse markers, there are two trees. We can see that the UDR can clearly draw the boundaries of the trees and their shadows. Note from this figure that, over the river, there are two bridges. The widths of the bridges are hand-labeled by 10 different experts. And then, the average width is computed and recorded as the true bridge width. For the left bridge, its true width is equal to 5.2-pixel width. For the right bridge, its true width is equal to 4.7-pixel width. From the detection result of each detector, we randomly select ten different positions to compute the detected width of the bridge. The results are shown in Table I. The detection result shown in Table I indicates that the bridges' widths obtained with the UDR are the best approximation to the real widths of the bridges. The bridges widths obtained by the edge detectors of RBED, GGS, ROEWA and ROA have been expanded by different degrees. This demonstrates that our proposed UDR has good

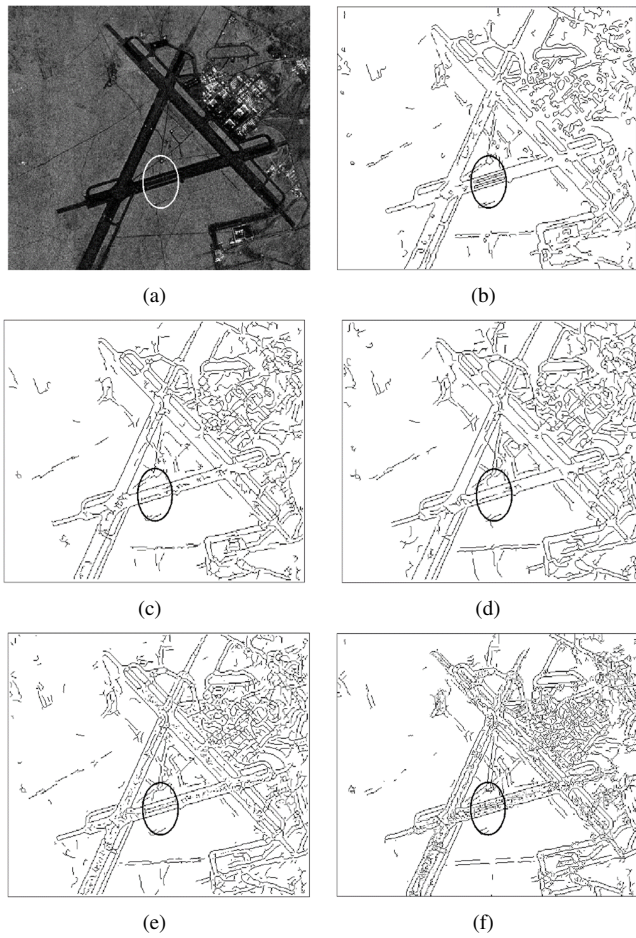


Fig. 12. Comparison of different detectors on real world SAR images. (a) China Lake Airport, California as observed by SAR (3-m resolution). Binary edge maps obtained by (b) UDR, (c) GGS, (d) RBED, (e) ROEWA, (f) ROA.

localization precision.

Interestingly, from the integrity of bridge, the detection result of UDR seems to be worse than the other detectors. For the sake of clarity, the region of right bridge is zoomed in and shown in Figure 14. From vision, there exists a crack on the bridge. However, common sense suggests that the bridge is likely to intact. This means there exists some conflicts between subjective assessment and objective result. Figures 14(b) and (c) are the detection results of UDR with different flat parameters. By enlarging this flat parameter $l_{||}$ of UDR, the integrity of bridge detected by UDR has been obviously improved. This suggests that UDR has ability to keep the integrity of bridge. When enlarging the flat parameter, the widths of left and right bridge are also widened 0.1 pixels. As we known, good edge integrity is generally caused by good elongation. However, good elongation does not mean high localization accuracy. Hence, we need to trade-off the localization accuracy and elongation degree on the basis of images and applications. In this experiment, we focus on the localization accuracy.

TABLE I
THE WIDTHS OF THE BRIDGES

Detector Name	Left Bridge	Right Bridge
Ground Truth	5.2	4.7
UDR	5.4	4.7
GGs	5.9	5.4
RBED	5.9	5.2
ROEWA	6.3	6.1
ROA	6.6	6.4

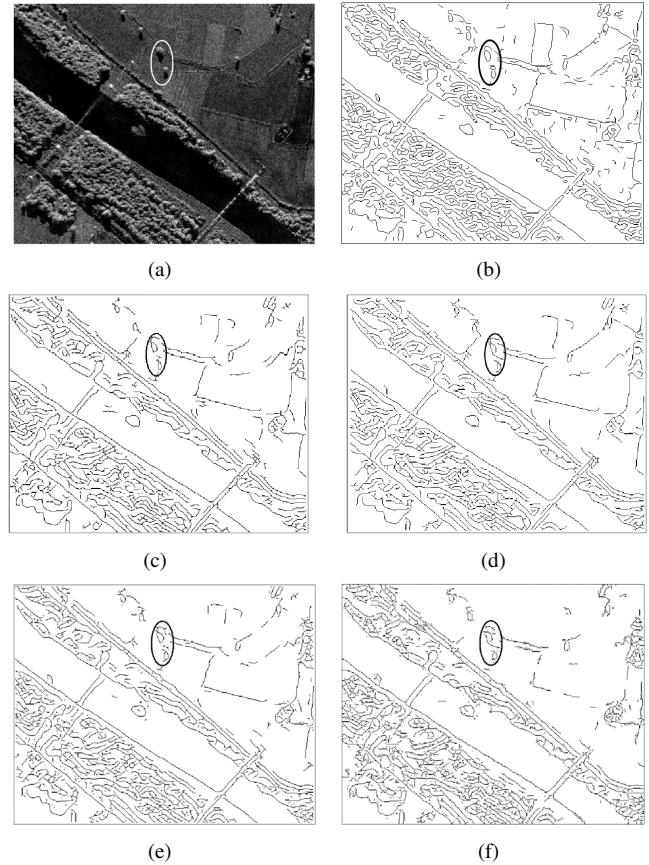


Fig. 13. Comparison of the binary edge maps obtained by UDR, GGS, RBED, ROEWA, and ROA edge detectors on real world SAR images with the same scene of Figure 10. (a) Amplitude-format of a real-world image with 1-m resolution from the Rio Grande River near Albuquerque. The binary edge maps obtained with the edge detectors of (b) UDR, (c) GGS, (d) RBED, (e) ROEWA, and (f) ROA respectively.

Another real-world SAR image coming from the website of InfoTerra/TerraSAR initiative is adopted to compare the detectors. Figure 15(a) shows a 500×500 amplitude-format real-world SAR image. It is from Pima County in USA (1-m resolution). The detection results are shown in Figure 15. Comparing with other detectors, UDR shows more detailed edges. For tiny objects in the upper-middle part of the image, UDR shows identifiable edge detection results. The ellipse marker marks a dark region. We can see that UDR accurately locates the edges of dark region. The detected edges of UDR have no obvious distortion, while the edges of other compared detectors show unignorable bias.

Section III.B and Section III.C have shown the theoretical proof that the simplified UDR is equivalent to UDR. All experiments shown in Section V are performed by UDR and

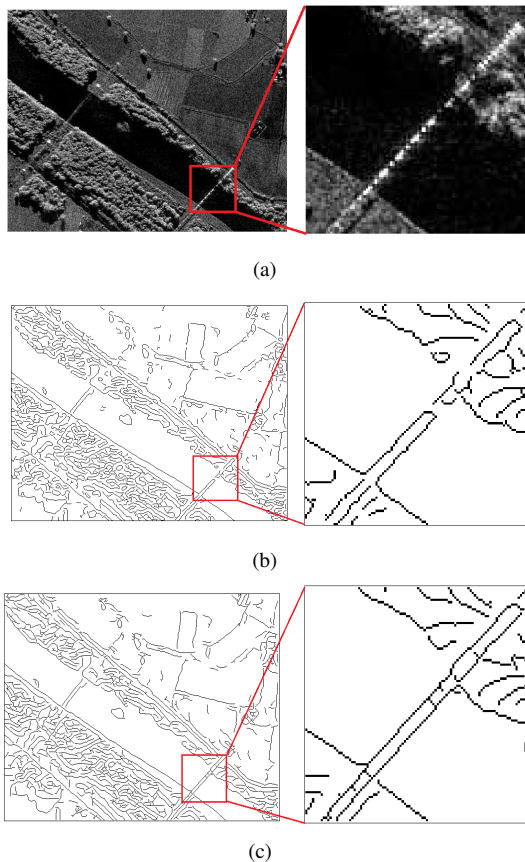


Fig. 14. Comparison of the binary edge maps obtained by UDR with different flat parameters. (a) Real world SAR image with same scene as Figure 13. The binary edge maps obtained by UDR with (b) flat parameter $l_{||} = 3$, and (c) flat parameter $l_{||} = 5$.

the simplified UDR. The two detectors show almost exactly the same experimental results, which are the experimental proof that the simplified version of UDR is equivalent to UDR. Since the experimental results obtained by two detectors are same, only the detection results of UDR are shown. The experiments illustrate the effectiveness of UDR and the simplified UDR.

V. CONCLUSIONS

In this paper, aiming to address the edge detection problem of step edges of SAR images with speckle noise, we have proposed a novel unbiased difference-ratio (UDR) edge detector with a unique detection structure, which integrates the difference operation with ratio operation. Theoretical analysis and experimental results have proved or demonstrated that the special structure makes UDR possess the properties of unbiased localization and constant false alarm rate (CFAR). The unbiased localization property is mainly due to the difference operation, while the CFAR is due to ratio operation part. It is the first time such the special structure has been designed and used for SAR edge detection. Experimental results show that the localization precision of the proposed detector is robust to the change of transition zone and the proposed UDR is insensitive to the change of edge contrast. Both objective and subjective experiments have demonstrated that the proposed UDR has a high true positive detection rate and low false



Fig. 15. Comparison of the binary edge maps obtained by UDR, GGS, RBED, ROEWA, and ROA edge detectors on real-world SAR images. (a) Amplitude-format of a real-world image with 1-m resolution from the Pima County in USA. The binary edge maps obtained with the edge detectors of (b) UDR, (c) GGS, (d) RBED, (e) ROEWA, and (f) ROA respectively.

alarm rate, superior to the state-of-the-art methods. To further improve the computational efficiency, a simplified version of UDR has been proposed by removing the parameter estimation step.

In our experiments, we find that the proposed edge detector has a capability to detect edge-line segments in SAR images. One of our future works is to study how to use such capability effectively. The proposed detector applies to step edges. A real-world SAR image usually contains many types of edges, such as ridge edge, ramp edge, step edge and so on. How to simultaneously detect edges of different types is another important question to be studied in the future. The solution of the question will largely broaden the availability of SAR edge detector.

APPENDIX A

In the Appendix A, ROA is used as an example to briefly explain the reason why traditional ratio-based edge detectors are

bias for step edges. Among ratio-based edge detectors, ROA introduced by Touzi is the most influential and representative one [14]. ROA uses a 2D separable edge detection filter to compute its edge strength map. The 2D separable detection filter $h_{ROA}(x, y)$ of ROA is as follows.

$$\begin{aligned} h_{ROA}(x, y) &= h_{MF}^{\perp}(|x|)h_{MF}^{\parallel}(y) \\ &= h_{MF}^{\perp}(x)h_{MF}^{\parallel}(y) + h_{MF}^{\perp}(-x)h_{MF}^{\parallel}(y) \end{aligned} \quad (\text{A.1})$$

where $h_{MF}^{\perp}(x)$ is a 1D rectangle (or mean) vertical filter and $h_{MF}^{\parallel}(y)$ is a 1D parallel filter. The formulation of ROA is shown in equation (34). Parameters of $h_{ROA}(x, y)$ control the support area (i.e. filter size) and they must take positive integer.

The 2D detection filter is represented as the direct product of a 1D vertical filter and a 1D parallel filter, in which the parallel filter is used to smooth images, while the vertical filter determines the statistic of an edge. In order to simply analyze the cause of bias, $h_{MF}^{\perp}(|x|)$ is directly performed on a 1D step edge. When $h_{MF}^{\perp}(|x|)$ performs on then edge shown in Figure 2(b) and moves within the transition zone $x \in [-a, a]$, the estimated edge position \hat{x} is evaluated by

$$\hat{x} = \arg \max_{x_0} (P_2(x_0)/P_1(x_0)) \quad (\text{A.2})$$

where $P_1(x_0)$ and $P_2(x_0)$ are the two local weight averages computed by $f_{MF}^{\perp}(x)$ and $f_{MF}^{\perp}(-x)$, respectively. Concretely speaking, the value of $P_2(x_0)/P_1(x_0)$ is computed by

$$\begin{aligned} \frac{P_2(x_0)}{P_1(x_0)} &= \frac{\int_{-\infty}^0 I_E(x_0 + x)h_{MF}^{\perp}(-x) dx}{\int_0^{+\infty} I_E(x_0 + x)h_{MF}^{\perp}(x) dx} \\ &= \frac{\mu_1 + \int_{-x_0-a}^0 (I_E(x_0 + x) - \mu_1)h_{MF}^{\perp}(-x) dx}{\mu_2 + \int_0^{a-x_0} (I_E(x_0 + x) - \mu_2)h_{MF}^{\perp}(x) dx} \end{aligned} \quad (\text{A.3})$$

Here, $\int_0^{+\infty} h_{MF}^{\perp}(x) dx = \int_{-\infty}^0 h_{MF}^{\perp}(-x) dx = 1$ is preserved. Conditions $I_E(-a)/\mu_1 - 1 = 0$ and $I_E(a)/\mu_2 - 1 = 0$ have been used.

With the help of Figure 2(a) and (b) and a phenomenological model [30], let the differential of $P_2(x_0)/P_1(x_0)$ with respect to x_0 be equal to zero and ignore the second order terms, and then we have Equation (A.4). In this equation, expression $\partial I(x_0)/\partial x_0 = (\mu_1 - \mu_2)\zeta(x_0)/2a$ for $x_0 \in [-a, a]$ is taken, where $\zeta(\bullet)$ denotes multiplicative noise with unit mean. Since $\mu_2 > \mu_1$, it is seen from Equation (A.4) that we must have

$$\int_0^{x_0+a} h_{MF}^{\perp}(x)\zeta(x_0 - x) dx < \int_0^{a-x_0} h_{MF}^{\perp}(x)\zeta(x_0 + x) dx. \quad (\text{A.5})$$

In order to keep the above inequality, the length of integrating interval $[0, a + x_0]$ must be smaller than that of integrating interval $[0, a - x_0]$ in most instances or in the statistical sense. Hence, the expected value of x_0 must satisfy $E\{x_0\} < 0$. Consequently, the edge position estimated by $h_{MF}^{\perp}(|x|)$ is biased, and tends towards to the darker side.

Similarly, when RBED, GGS and ROEWA are performed on nonideal edges, the estimated edge positions are biased.

Among these detectors, RBED has smallest bias [17]. Refer to literature [17] for further information on bias analysis of RBED.

ACKNOWLEDGMENT

The authors would like to thank...

REFERENCES

- [1] L. Dias, F. Cribari-Neto, and R. Ospina, "Interval Edge Estimation in SAR Images," *IEEE Transactions on Geoscience and Remote Sensing*, vol. 52, pp. 851-861, 2015. DOI: 10.1109/TGRS.2014.2329140
- [2] Jiange Liu, K. Andrea Scott, Ahmed Gawish and Paul Fieguth, "Automatic Detection of the Ice Edge in SAR Imagery Using Curvelet Transform and Active Contour," *Remote Sensing*, vol. 8, pp. 480, 2016. DOI: 10.3390/rs8060480
- [3] Yuming Xiang, Feng Wang, Ling Wan and Hongjian You, "SAR-PC: Edge detection in SAR image via an advanced Phase Congruency Model," *Remote Sensing*, vol. 9, pp. 209, 2017. DOI: 10.3390/rs9030209
- [4] X. I. Ma, S. Q. Liu, and S. H. Hu et al., "SAR Image Edge Detection via Sparse Representation," *Soft Computing*, vol. 22, no. 8, pp. 2507-2515, 2018. DOI: 10.1007/s00500-017-2505-y
- [5] Song Tu and Yi Su, "Fast and Accurate Target Detection Based on Multiscale Saliency and Active Contour Model for High-Resolution SAR Images," *IEEE Transactions on Geoscience and Remote Sensing*, vol. 54, no. 10, pp. 5729-5744, 2016.
- [6] Long Li, Francois-Xavier Le Dimet, Jianwei Ma, and Arthur Vidard, "A Level-Set-Based Image Assimilation Method: Potential Applications for Predicting the Movement of Oil Spills," *IEEE Transactions on Geoscience and Remote Sensing*, pp.1-14, 2017.
- [7] Linlin Xu, A. D. Clausi, FanLi, and Alexander Wong, "Weakly Supervised Classification of Remotely Sensed Imagery Using Label Constraint and Edge Penalty," *IEEE Transactions on Geoscience and Remote Sensing*, vol. 55, pp. 1424-1436, 2017. DOI: 10.1109/TGRS.2016.2623942
- [8] C. Liu, Y. Xiao, and J. Yang, "A Coastline Detection Method in Polarimetric SAR Images Mixing the Region-Based and Edge-Based Active Contour Models," *IEEE Transactions on Geoscience and Remote Sensing*, vol. 55, pp. 3735-3747, 2017.
- [9] X. Tang, L. Jiao, and W. J. Emery, "SAR Image Content Retrieval Based on Fuzzy Similarity and Relevance Feedback," *IEEE Journal of Selected Topics in Applied Earth Observations and Remote Sensing*, pp. 1-19, 2017.
- [10] J. Chen, C. Wang, H. Zhang, et al. "Automatic Detection of Low-Rise Gable-Roof Building from Single Submeter SAR Images Based on Local Multilevel Segmentation," *Remote Sensing*, vol. 9, pp. 263, 2017. DOI: 10.3390/rs9030263
- [11] M. Petrou, and J. Kittler, "Optimal Edge Detectors for Ramp Edges," *IEEE Transactions on Pattern Analysis and Machine Intelligence*, vol. 13, pp. 483-495, 1996. DOI: 10.1109/34.134047
- [12] J. Canny, "A Computational Approach to Edge Detection," *IEEE Transactions on Pattern Analysis and Machine Intelligence*, vol. 8, pp. 679-698, 1986. DOI: 10.1109/TPAMI.1986.4767851
- [13] M. Amirmazlaghani, H. Amindavar, and A. Moghaddamjoo, "Speckle Suppression in SAR Images Using the 2-D GARCH Model," *IEEE Transactions on Image Processing*, vol.18, pp. 250-295, 2008. DOI: 10.1109/TIP.2008.2009857
- [14] R. Touzi, A. Lops, and P. Bousuet, "A Statistical and Geometrical Edge Detector for SAR Images," *IEEE Transactions on Geoscience and Remote Sensing*, vol. 26, pp. 764-773, 1988. DOI: 10.1109/36.7708
- [15] R. Fjrtoft, A. Lops, P. Marthon, and E. Cubero-Castan, "An Optimal Multiedge Detector for SAR Image Segmentation," *IEEE Transactions on Geoscience and Remote Sensing*, vol. 36, pp. 793-802, 1988. DOI: 10.1109/36.673672
- [16] P. L. Shui, and D. Cheng, "Edge Detector of SAR Image Using Gaussian-Gamma-shaped Bi-Windows," *IEEE on Geoscience and Remote Sensing Letters*, vol. 9, pp. 846-850, 2012. DOI: 10.1109/LGRS.2012.2184521
- [17] Q. R. Wei, and D. Z. Feng, "An Efficient SAR Edge Detector with a Lower False Positive Rate," *International Journal of Remote Sensing*, vol. 36, pp. 3773-3797, 2015. DOI: 10.1080/01431161.2015.1054046
- [18] H. Zhang, W. Ni and W. Yan, et al., "Robust SAR Image Registration Based on Edge Matching and Refined Coherent Point Drift," *IEEE Geoscience and Remote Sensing Letters*, vol. 12 no.10, pp.2115-2119, 2015. DOI: 10.1109/LGRS.2015.2451396

$$\begin{aligned}
0 &= \mu_2 \int_{-x_0-a}^0 h_{MF}^\perp(-x) \zeta(x_0-x) dx - \mu_1 \int_0^{a-x_0} h_{MF}^\perp(x) \zeta(x_0+x) dx \\
&= \mu_2 \int_0^{x_0+a} h_{MF}^\perp(x) \zeta(x_0-x) dx - \mu_1 \int_0^{a-x_0} h_{MF}^\perp(x) \zeta(x_0+x) dx
\end{aligned} \tag{A.4}$$

- [19] P. Dare and I. Dowman, "A New Approach to Automatic Feature Based Registration of SAR and SPOT Images," *Isprs Journal of Photogrammetry and Remote Sensing*, vol. xxxiii, no. 1, pp. 1328, 2000.
- [20] M. Akshaya, W. Alexander, "KPAC: A Kernel-Based Parametric Active Contour Method for Fast Image Segmentation," *IEEE Signal Processing Letters*, vol. 17, pp. 312-315, 2010. DOI: 10.1109/LSP.2009.2036654
- [21] Y. L. Chang, Z. M. Zhou, W. G. Chang, and T. Jin, "New Edge Detection Method for High-Resolution SAR Images," *Journal of Systems Engineering and Electronics*, vol. 17, pp. 316-320, 2006. DOI: 10.1016/S1004-4132(06)60055-8
- [22] C. J. Oliver, I. McConnell, D. Blacknell, and R. G. White, "Optimum Edge Detection in SAR," *JIEE Proceedings - Radar, Sonar and Navigation*, vol. 143, pp. 31-40, 1995. DOI: 10.1049/ip-rsn:19960219
- [23] L. Vincent and P. Soille, "Watersheds in Digital Spaces: An Efficient Algorithm Based on Immersion Simulations," *IEEE Transactions on Pattern Analysis and Machine Intelligence*, vol. 13, pp. 583-598, 1991. DOI: 10.1109/34.87344
- [24] O. Germain, and P. Rfgrier, "Optimal Snake-Based Segmentation of a Random Luminance Target on a Spatially Disjoint Background," *Optics Letters*, vol. 21, pp. 1845-1847, 1996. DOI: 10.1049/ip-rsn:19960219
- [25] X. Fu, H. You, and K. Fu, "A Statistical Approach to Detect Edges in SAR Images Based on Square Successive Difference of Averages," *IEEE Geoscience and Remote Sensing Letters*, vol. 9, pp. 1094-1098, 2012. DOI: 10.1109/LGRS.2012.2190378
- [26] A. Lops, R. Fjrtoft, and D. Ducrot, "Edge Detection and Segmentation of SAR Images in Homogeneous Regions," In *Information processing for remote sensing*; C. H. Chen, Ed.; Singapore: World Scientific, 1999; pp. 139-166, ISBN: 978-981-02-3737-0
- [27] O. Germain, and P. Rfgrier, "Edge Location in SAR Images: Performance of the Likelihood Ratio Filter and Accuracy Improvement with an Active Contour Approach," *IEEE Transactions on Image Processing*, vol. 10, pp. 72-78, 2001. DOI: 10.1109/83.892444
- [28] A. C. Frery, H. J. Muller, C. F. Yanasse, and S. J. Anna, "A Model for Extremely Heterogeneous Clutter," *IEEE Transactions on Geoscience and Remote Sensing*, vol. 35, pp. 648-659, 1997. DOI:10.1109/36.581981
- [29] H. Allende, A. C. Frery, J. Galbiati, and L. Pizarro, "M-estimators with Asymmetric Influence Functions: The GA0 distribution case," *Journal of Statistical Computation and Simulation*, vol. 76, pp.941-956, 2006. DOI: 10.1080/10629360600569154
- [30] O. Germain, and P. Rfgrier, "On the Bias of the Likelihood Ratio Edge Detector for SAR Images," *IEEE Transactions on Geoscience and Remote Sensing*, vol. 38, pp. 1445-1457, 2000. DOI: 10.1109/36.843041
- [31] X. Zhang, X. Wen, and H. Xu et al., "Synthetic Aperture Radar Image Segmentation Based on Edge-Region Active Contour Model," *Journal of Applied Remote Sensing*, vol. 10, 2016.
- [32] U. Javed, M. M. Riaz, and A. Ghafoor, et al., "SAR Image Segmentation Based on Active Contours with Fuzzy Logic," *IEEE Transactions on Aerospace and Electronic Systems*, vol. 52, pp. 181-188, 2016.
- [33] S. V. Frost, and A. S. Josphine, "A Model for Radar Images and Its Application to Adaptive Digital Filtering of Multiplicative Noise," *IEEE Transactions on Pattern Analysis and Machine Intelligence*, vol. 4, pp. 157-166, 1982. DOI: 10.1109/TPAMI.1982.4767223
- [34] M. K. Tur, C. Chin, and J. W. Goodman, "When Is Speckle Noise Multiplicative," *Applied Optics*, vol. 21, pp. 1157-1159, 1982. DOI: 10.1364/AO.21.001157
- [35] Y. Cui, G. Zhou, J. Yang, and Y. Yamaguchi, "Unsupervised Estimation of the Equivalent Number of Looks in SAR Images," *IEEE Geoscience and Remote Sensing Letters*, vol. 8, pp. 710-714, 2011. DOI: 10.1109/LGRS.2010.2102335
- [36] S. N. Anfinsen, A. P. Doulgeris, and T. Eltoft, "Estimation of the Equivalent Number of Looks in Polarimetric Synthetic Aperture Radar Imagery," *IEEE Transactions on Geoscience and Remote Sensing*, vol. 47, pp. 3795-3809, 2009. DOI: 10.1109/TGRS.2009.2019269
- [37] K. R. Rao, and A. J. Ben, "Optimal Edge Detection Using Expansion Matching and Restoration," *JIEE Transactions on Pattern Analysis and Machine Intelligence*, vol. 16, pp. 1169-1182, 1994. DOI: 10.1109/34.387490
- [38] I. E. Abdou, and W. K. Pratt, "Quantitative Design and Evaluation of Enhancement/Thresholding Edge Detectors," *Journal Abbreviation*, vol. 67, pp. 753-763, 1979. DOI: 10.1109/PROC.1979.11325
- [39] W. K. Pratt, "Digital Image Characterization," In *Digital Image Processing*; John Wiley, Sons, Eds.; A Wiley-Interscience Publication, New York: Wiley, 1978; ISBN: 0-471-01888-0
- [40] K. Bowyer, C. Kranenburg, and Dougherty, "Edge Detector Evaluation Using Empirical ROC Curves," *Computer Vision and Image Understanding*, vol. 84, pp. 77-103, 2001. DOI: 10.1006/cviu.2001.0931
- [41] M. Heath, S. Sarker, T. Sanocki, and K. W. Bowyer, "Comparison of Edge Detectors: A Methodology and Initial Study," *IEEE Computer Society Conference on Computer Vision and Pattern Recognition*, vol. 69, pp.143-148, 1996. DOI: 10.1109/CVPR.1996.517066
- [42] Y. Lu, Q. Gao, and D. Sun, et al., "Directionlet-Based Method using the Gaussian Mixture Prior to SAR Image Despeckling," *International Journal of Remote Sensing*, vol. 35, no. 3, pp. 1143-1161, 2014.
- [43] M. Petrou, "Separable 2-D Filters for the Detection of Ramp Edges," *IEE Proceedings-Vision, Image and Signal Processing*, vol. 142, no. 4, pp. 228-231, 1995.
- [44] Rafael C. Gonzalez, Richard E. Woods and Steven L. Eddins, "Digital Image Processing Using MATLAB (Second Edition)," Publishing House of Electronics Industry, China: Beijing, 2013; ISBN: 9787121195440